N68 25724

FINAL REPORT
FOR
DYNAMIC STABILITY STUDY
FOR
SOUNDING ROCKETS

CONTRACT NO.: NAS 5-10438

LMSC 684879

January 1968

Written by D. A. Price, Jr.

P. S. Woods

Approved M. Tucker, Manager
Flight Technology

Prepared By

Lockheed Missiles & Space Company
1111 Lockheed Way
Sunnyvale, California

for

Goddard Space Flight Center
Greenbelt, Maryland

ABSTRACT

This report presents the results of an investigation of the effects of joint rotation and compliance, body flexibility, fin flexibility, and induced and non-linear aerodynamic characteristics on roll resonance behavior of sounding rockets.

Maximum tolerance limits for center of gravity, aerodynamic trim and thrust misalignment with joint rotation or "slop" and body bending (including joint compliance) are compared with those for a rigid vehicle for time variable linear aerodynamics. Application to the Aerobee 150 flight number 4.81 vehicle with twelve joints, is made to demonstrate that joint rotation can provide a major source of roll lock-in. The character of the flight behavior was satisfactorily simulated.

A specially developed computer program (FLEXCOR) for evaluating multiple-jointed, body extensions which is applicable to sounding rockets in general is utilized. A method for accommodating fin flexibility effects is developed and a unified computation procedure suitable for the FLEXCOR program formulated.

Induced and non-linear aerodynamics are shown to cause significant but acceptable reduction in asymmetry tolerances for a rigid body Aerobee 350 sounding rocket. Modifications to the existing Roll Pitch Motion (RPM) program to accommodate induced and non-linear aerodynamic characteristics in the dynamic motion and c.g. tolerance options are described.

TABLE OF CONTENTS

Section 1
INTRODUCTION

1.1 Background

The investigation described in this report represents an extension of theory and techniques developed in previous studies on roll resonance phenomena for sounding rockets. The basic understanding and exposition of the sources and mechanisms of roll resonance phenomena leading to roll lock-in were developed in ref. 1 for rigid vehicles with linear aerodynamic characteristics. It was demonstrated that the primary source of roll lock-in was the coupling between the lateral center of gravity offset and the aerodynamic normal force resulting from the pitch resonant response to trim asymmetries. Definition of roll lock-in criterion based on steady state behavior led to simple and precise specification of asymmetry tolerances in terms of an effective aerodynamic trim asymmetry C_{m_o}, an effective thrust misalignment ϵ, and an effective center of gravity lateral offset Δcg.

A specialized computer program (ref. 2) was developed to provide economical calculation of these tolerances and to illustrate the dynamic motion behavior of the sounding rocket under the influence of such asymmetries. Comparison with flight results and comprehensive 6-D simulations (ref. 3) including non-linear aerodynamics and aeroelastic effects demonstrated the efficacy of the equilibrium solutions developed in refs. 1 and 4.

Reference 5 explored methods for providing positive roll control in the the presence of configuration, mass, and thrust asymmetries. Significant improvement in roll lock-in tolerance was found for simple control devices plus significant reduction angle-of-attack response during passage through resonance.

Asymmetry tolerance criteria for limiting motion behavior during the experiment or prior to attitude control acquisition were developed in the studies of ref. 6. An examination of the relative importance of the mechanisms causing roll lock-in identified the fin characteristics as the most critical aerodynamic derivatives.

The effects of vehicle flexibility upon roll resonance behavior was explored also in ref. 6 by defining and evaluating aeroelastic corrections to the rigid body aerodynamic characteristics and asymmetries. Changes in the roll lock-in tolerance contour were then evaluated with approximate solutions. The rigid body contours were modified and assessed with equivalent rigid body dynamic trajectory calculations. It was shown that the principal role of vehicle bending is to extend roll resonance through an aeroelastic increase in the extant asymmetries. A computer program (FLEXCOR) was devised (ref. 7) to carry out the complex matrix operations used to describe the flexing vehicle using precomputed twist and bending modes with c.g. offset, thrust, and trim asymmetries, angular motion from the RPM program and rigid body linear aerodynamics.

A preliminary examination of the effects of rotational play in the joints between sustainer, body extensions, and nose shroud identified a potential source of large aerodynamic trim asymmetries which should be investigated in more detail.

The investigations of ref. 6 developed a better understanding of the effects of vehicle flexibility on roll resonance phenomena and pointed out the need for refinement of the analysis methods and suitable tools for precise and economical evaluation of other sounding rockets.

A basic assumption of the previous studies (refs. 1, 3, 4, and 6) was that small angle-of-attack linear aerodynamics except for the induced roll moment were sufficient to specify adequate asymmetry tolerances. Other studies (refs. 3, 8, and 9 as well as 4) have shown that the unsymmetric induced side forces and moments and the basic symmetric non-linear characteristics can change the dynamic motion behavior significantly. Hence, an evaluation of these flow interactions upon asymmetry tolerance criteria was in order.

The present study was undertaken to fulfill these needs.

1.1 Study Objectives

The overall objective of this study was to determine the effects of multiple-jointed body extensions, fin flexibility and flow induced aerodynamic interactions on roll resonance behavior leading to roll lock-in. More specific objectives are listed below:

- Investigate body joint rotation as a source of roll lock-in
- Mechanize calculation of equivalent rigid body force and moment increments due to vehicle bending and joint slop and compliance
- Determine equivalent rigid body asymmetry tolerances for the Aerobee 150 vehicle and compare with flight #4.81 behavior
- Develop a method for determining incremental forces and moments for a flexible fins – plus – body system suitable for incorporation in the FLEXCOR program
- Conduct a preliminary investigation of the effects of vehicle flexibility on induced rolling moment characteristics
- Develop a description of flow induced side forces and moments applicable to the body-axis system used in the Roll Pitch Motion (RPM) computer program
- Modify the RPM program to incorporate induced and non-linear aerodynamic characteristics into the dynamic motion and center of gravity tolerance options
- Determine asymmetry tolerance contours with induced and non-linear aerodynamics for the Aerobee 350 sounding rocket vehicle

1.3 Technical Approach

The overall philosophy invoked in the investigation was to provide an understanding of the important phenomena, develop cogent methods and tools for analysis appropriate for sounding rockets in general, and to illustrate the application of these procedures with representative vehicle.

The basic methods developed in refs. 1, 2, 4, 5, and 6 were utilized for this investigation with primary emphasis on motion response at small angles of attack. The

steady state or equilibrium resonant response of the spinning rocket was used to define roll lock-in criterion and establish tolerances to trim and mass asymmetries. The procedure has been shown to yield conservative asymmetry tolerances when time varying environment, dynamic motion response,and inertial properties of the vehicle are included.

Aeroelastic corrections to the rigid body aerodynamic characteristics, trim asymmetry, and thrust misalignment are determined from the trimmed deflections while in roll resonance. Structural oscillations about trim deflections are neglected in the same sense that the rigid body oscillatory motions about the trim angle of attack are neglected. The aeroelastic effects are couched in terms of "effective" rigid body characteristics for definition of preflight asymmetry tolerances. The usual linearizations are employed in the structural analysis to realize tractable solutions.

Linear aerodynamic characteristics except for the induced rolling moment were adequate in all of the prior studies for explaining the phenomena and assessing small angle behavior. Departures from a linear representation is approached with the same basic resonant trim method used for the linear case but with appropriate modification in the computation procedures.

1.4 Plan of the Report

The important results of the investigations made during the study are summarized in the following sections of this report. The body bending and joint rotation analyses are described in Section 2. The development of a method for evaluating fin flexibility effects on roll resonance behavior is traced in Section 3. Section 4 presents the analyses conducted on the influence of induced and non-linear aerodynamic characteristics on rigid body asymmetry tolerances and motion behavior. The preliminary examination of the effects of body bending on induced rolling moment characteristics is summarized in Section 5. Conclusions emerging from the investigations and suggestions for further study are reviewed in Section 6.

Section 2

ROLL RESONANCE WITH MULTIPLE JOINT BODY EXTENSIONS

In Reference 6, an analysis of body flexibility for a spinning vehicle was made to determine the effects upon the behavior of the vehicle in a state of equilibrium roll resonance. Such effects for the Aerobee 350 including both elastic body bending and body twisting were shown to be measurably, though not dramatically significant in altering the allowable e.g. offset tolerance contours.

In the present analysis, the effects of multiple-joint body extensions are investigated. For this purpose, the Aerobee 150 vehicle, Flight No. 4.81 was selected as an extreme case in which the body contains twelve points. This is depicted in Fig. 1. The mechanical characteristics of the joints used in this vehicle are shown in the figure by the sketch of moment across the joint, M_j vs. joint rotation θ. "Sloppy" joints are characterized by relative rotation of two mating cylindrical body sections under zero load. Further rotation is idealized as a linear function of load; that is, as a linear compliance.

2.1 MODEL OF ELASTIC VEHICLE

A model of the elastic vehicle is depicted in Fig. 2 where the undeflected elastic axis is shown by the ξ, η, ζ coordinate axes. The equations of motion for a spinning vehicle are derived in Ref. 6 to include bending in the normal and lateral planes as well as twisting about the longitudinal axis. These equations are derived with respect to a reference axis system arbitrarily located anywhere in the vehicle. The purpose of an arbitrary axis location is to allow bending and twist modes to be structurally uncoupled by choosing the reference ξ-axis to be coincident with the elastic axis.

In the derivation described in Ref. 6 the elastic modes were computed separately with respect to the elastic axis. When combined into the over-all equations of motion, mass-coupling terms appear for any center-of-gravity offset.

The analysis presented here makes use of the same equations of motion developed in Ref. 6. There is no change in the form of the equations. Joint compliance, previously neglected in the origianl derivation, is represented in Fig. 2 by the little spiral springs located across pinned joints connecting the elastic beams of the mathematical model. Between the beams are lumped blocks of mass. Elastic bending modes are computed for this model as though there is zero slop in the joint. This procedure is permissable in place of computing the modes for a non-linear joint (as shown in Fig. 1) since, in a condition of equilibrium roll resonance, the equations of motion are steady-state. The effects of slop; that is, joint rotation are included in the aerodynamic force inputs.

2.2 EQUATIONS OF MOTION

Derivation of the steady-state equations for equilibrium roll resonance proceeds from consideration of all the forces on a single mass point as indicated in Ref. 6. The elastic displacements of each mass point in the vehicle are represented by the components ξ, η, ζ in the x, y, z directions respectively. For all mass points, the elastic displacements are represented by the symbol

$$\left|\left|\begin{matrix}\xi\\ \eta\\ \zeta\end{matrix}\right|\right|$$

which may be visualized as a column of three-element columns. The motion of mass points distributed throughout the vehicle is replaced by the model of Fig. 2 for the purpose of computing bending and twist modes*. Free-free elastic modal displacements $\hat{\varphi}_i$, $\hat{\eta}_i$, and $\hat{\varphi}_i$ are computed for each block of mass corresponding to twist,

*Twist modes are computed on the basis of zero compliance across the joints; i.e. infinite torsional stiffness

lateral bending and normal bending, respectively. Finally, these modal displacements are related to mass point displacements by replacing each block of mass in Fig. 2 with an equivalent set of five discrete mass points as shown in Fig. 3. A minimum of five discrete mass points are required to represent five known mass properties of each block, namely:

m = total mass of block

σ_y = static unbalance of block from x-z plane

σ_z = static unbalance of block from x-y plane

i_y^y = moment of inertia of block about y-axis

i_z^z = moment of inertia of block about z-axis

Four of the mass points are taken at vehicle radius r and the fifth mass point at the elastic axis. Lift forces are assumed to act at the centeral mass point. At the fin, the four outboard mass points are taken at a radius coincident with the center of pressure of each fin and aerodynamic forces resulting from fin cant are applied at these points. The sets of mass points shown in Fig. 3 are assumed to remain coplanar at all times.

The modal displacement for each mass point is constructed from bending and twist modes by the relation

$$\begin{vmatrix} \hat{\xi} \\ \hat{\eta} \\ \hat{\zeta} \end{vmatrix} = \begin{vmatrix} \hat{0} \\ \hat{\eta} \\ \hat{\zeta} \end{vmatrix} + \begin{bmatrix} 0 & z & -y \\ -z & 0 & 0 \\ y & 0 & 0 \end{bmatrix} \begin{vmatrix} \hat{\varphi} \\ \hat{\theta} \\ \hat{\psi} \end{vmatrix}$$

mass point location from elastic axis

Block rotation

Displacement of one block (Fig. 2)

One mass point

This manipulation is required in order to construct the matrix of generalized strain for each block of mass defined as

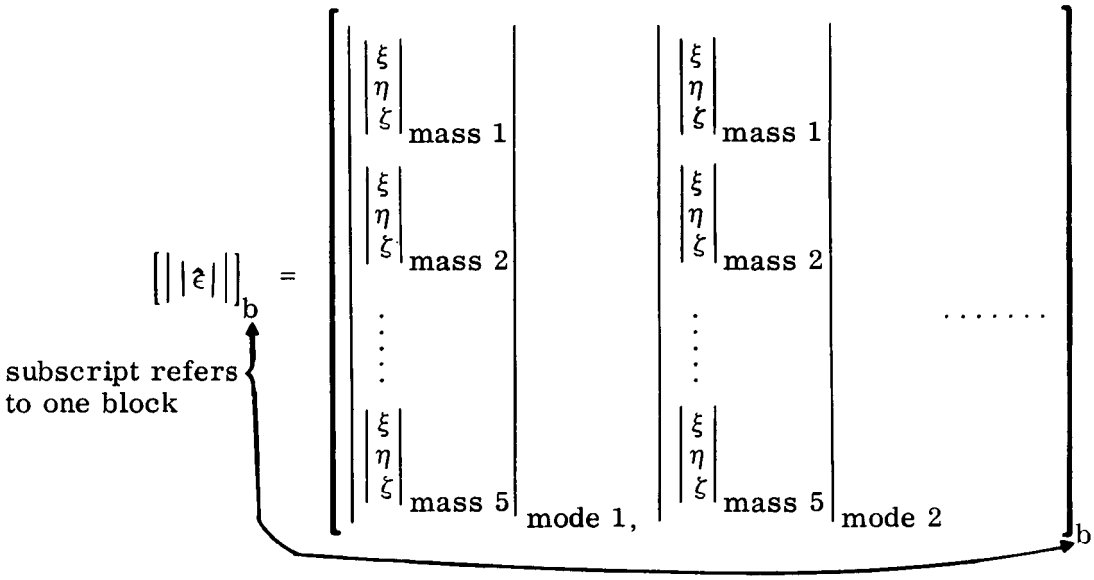

The equations of motion derived in Ref. 6 are summarized in Fig. 4. The assumptions underlying the steady state solution are shown in Fig. 5 and the resulting solution is shown in Fig. 6. The matrix operations indicated in Fig. 6 are carried out one block at a time using the generalized strain matrix, $||\hat{\epsilon}||$ or its transpose $\{\{\hat{\epsilon}\}\}$, as defined above. The results are summed for all blocks to yield the final form shown below:

$$\left[[F][E]^{-1}[A] - [B]\right] \left|\begin{matrix} |\bar{\gamma}| \\ |\omega| \end{matrix}\right| = |D| - [F][E]^{-1}|C|$$

rigid body

elastic increment to life and moment

Thus, incremental lift forces and moments due to elastic bending and joint rotation may be expressed as

$$\begin{bmatrix} \Delta L_\gamma \ , \ \Delta L_\omega \\ \Delta M_\gamma \ , \ \Delta M_\omega \end{bmatrix} = [F][E]^{-1}[A]$$

and

$$\begin{vmatrix} \Delta L_o \\ \Delta M_o \end{vmatrix} = [F][E]^{-1}|C|$$

where $[\Delta L_\gamma \ , \ \Delta L_\omega]$ = components of force in X, Y, and Z directions due to angle of attack and rotation rate

$$= \begin{bmatrix} \frac{\partial(\text{Drag})}{\partial\alpha} & , & \frac{\partial(\text{Drag})}{(-\beta)} & , & \frac{\partial(\text{Drag})}{\partial p} & , & \frac{\partial(\text{Drag})}{\partial q} & , & \frac{\partial(\text{Drag})}{\partial r} \\ \frac{\partial(\text{Side Force})}{\partial\alpha} & , & \frac{\partial(\text{Side Force})}{(-\beta)} & , & \frac{\partial(\text{Side Force})}{\partial p} & , & \frac{\partial(\text{Side Force})}{\partial q} & , & \frac{\partial(\text{Side Force})}{\partial r} \\ \frac{\partial(\text{Lift})}{\partial\alpha} & , & \frac{\partial(\text{Lift})}{(-\beta)} & , & \frac{\partial(\text{Lift})}{\partial p} & , & \frac{\partial(\text{Lift})}{\partial q} & , & \frac{\partial(\text{Lift})}{\partial r} \end{bmatrix}$$

and $[\Delta M_\gamma, \Delta M_\omega]$ = components of moment in X, Y, and Z directions due to angle of attack and rotation rate

$$= \begin{bmatrix} \frac{\partial\left(\begin{smallmatrix}\text{Roll}\\ \text{Moment}\end{smallmatrix}\right)}{\partial\alpha} & , & \frac{\partial\left(\begin{smallmatrix}\text{Roll}\\ \text{Moment}\end{smallmatrix}\right)}{\partial(-\beta)} & , & \frac{\partial\left(\begin{smallmatrix}\text{Roll}\\ \text{Moment}\end{smallmatrix}\right)}{\partial p} & , & \frac{\partial\left(\begin{smallmatrix}\text{Roll}\\ \text{Moment}\end{smallmatrix}\right)}{\partial q} & , & \frac{\partial\left(\begin{smallmatrix}\text{Roll}\\ \text{Moment}\end{smallmatrix}\right)}{\partial r} \\ \frac{\partial\left(\begin{smallmatrix}\text{Pitch}\\ \text{Moment}\end{smallmatrix}\right)}{\partial\alpha} & , & \frac{\partial\left(\begin{smallmatrix}\text{Pitch}\\ \text{Moment}\end{smallmatrix}\right)}{\partial(-\beta)} & , & \frac{\partial\left(\begin{smallmatrix}\text{Pitch}\\ \text{Moment}\end{smallmatrix}\right)}{\partial p} & , & \frac{\partial\left(\begin{smallmatrix}\text{Pitch}\\ \text{Moment}\end{smallmatrix}\right)}{\partial q} & , & \frac{\partial\left(\begin{smallmatrix}\text{Pitch}\\ \text{Moment}\end{smallmatrix}\right)}{\partial r} \\ \frac{\partial\left(\begin{smallmatrix}\text{Yaw}\\ \text{Moment}\end{smallmatrix}\right)}{\partial\alpha} & , & \frac{\partial\left(\begin{smallmatrix}\text{Yaw}\\ \text{Moment}\end{smallmatrix}\right)}{\partial(-\beta)} & , & \frac{\partial\left(\begin{smallmatrix}\text{Yaw}\\ \text{Moment}\end{smallmatrix}\right)}{\partial p} & , & \frac{\partial\left(\begin{smallmatrix}\text{Yaw}\\ \text{Moment}\end{smallmatrix}\right)}{\partial q} & , & \frac{\partial\left(\begin{smallmatrix}\text{Yaw}\\ \text{Moment}\end{smallmatrix}\right)}{\partial r} \end{bmatrix}$$

Incremental drag forces are generally quite small and the first equation may usually be ignored. Other components are combined vectorially to determine the change in the rigid body derivatives.

Similarly

$$|\Delta L_o| = \text{Three components of constant forces}$$

$$= \Delta \begin{vmatrix} \text{Drag + Thrust} \\ \text{Force in lateral plane} \\ \text{Force in vertical plane} \end{vmatrix}$$

$$|\Delta M_o| = \Delta \begin{vmatrix} \text{Roll Moment} \\ \text{Pitch Moment} \\ \text{Yaw Moment} \end{vmatrix}$$

The rigid body components of constant force and moment are expressed in the form

$$|D| = \begin{vmatrix} \text{Drag + Thrust} \\ \text{Thrust misalignment in X-Y plane} \\ \text{Thrust misalignment in X-Z plane} \\ \text{Roll moment due to fin cant} \\ \text{Pitch moment due to } C_{m_o} \\ \text{Yaw moment due to } C_{m_o} \end{vmatrix}$$

"Worst" cases were examined in this investigation from the standpoint of selecting components of aerodynamic trim and thrust misalignment acting in perpendicular planes.

2.3 FLEXCOR PROGRAM

In Fig. 7 is shown a flow chart of the computer routines used to establish Δc.g. tolerances as functions of aerodynamic characteristics and thrust misalignment . Essentially, two routines are used. The RPM program establishes the rigid body motion; namely, α, β, p, q, r and the allowable rigid body c.g. offset. This is used as input to the FLEXCOR program along with stiffness, mass distribution and joint compliance, joint slop and aerodynamic normal force distribution modified by joint rotation. The calculation of the uncoupled bending and twist modes including the effects of joint compliance is programmed as an integral part of the FLEXCOR routine so that the generalized strain matrix, $[|\epsilon|]$, is automatically computed from the output of the modal calculations. This eliminates a laborious preparation of modal displacements for each block of mass in the elastic model of Fig. 2. Fin flexibility is discussed in Section 3 of this report but was not varied parametrically as an input to the numerical results obtained from the FLEXCOR routine. Output of the FLEXCOR routine is a six-by-six column matrix, $[F][E]^{-1}[A]$, and a six-by-one column matrix, $[F][E]^{-1}|C|$ as shown in Fig. 6. Aeroelastic corrections to the rigid body derivatives are then prepared manually for input to the RPM program. Two iteratative passes between RPM and FLEXCOR have been found adequate for defining asymmetry tolerances.

2.4 ASYMMETRY TOLERANCE CONTOURS FOR THE AEROBEE 150

The procedure described in the preceding sections was applied to the Aerobee 150 of Fig. 1 with the results presented in Fig. 8. The aerodynamic data of Ref. 21 except for induced roll moment was utilized. The rigid body calculations from the RPM program (Ref. 2) yield quite small ΔCG tolerances primarily due to the small fin cant angle (δ = 0.15 deg). This yields resonance at fairly high altitude (58,000 feet) where the fin driving moment is small.

Flexibility (including joint compliance) alone produces only minor reduction of the tolerances for an aerodynamic asymmetry. A very drastic degradation is caused by the joint rotation on "slop". The allowable intercept C_{m_o} is reduced by 43 percent

when the incremental ΔC_{m_o} is applied directly (Iteration No. 1). The aerodynamic characteristics are changed significantly as listed below:

$$\Delta C_{m_\alpha}/C_{m_\alpha} = -45 \text{ percent}$$

$$\Delta C_{N_\alpha}/C_{N_\alpha} = +77 \text{ percent}$$

$$\Delta C_{m_q}/C_{m_q} = +10 \text{ percent}$$

$$\Delta C_A/C_A = +1.5 \text{ percent}$$

$$\Delta C_{l_\delta}/C_{l_\delta} \quad \text{negligible}$$

$$\Delta C_{l_p}/C_{l_p} \quad \text{negligible}$$

Accounting for these changes in the RPM ΔCG calculation yields the curve label Iteration No. 2. Successive iterations between the RPM and FLEXCOR programs can be used to converge upon the contour with joint slop to the desired degree of accuracy. The second iteration indicates a 32 percent reduction in the allowable rigid body intercept C_{m_q}.

The reduction of the allowable thrust misalignment is large for body bending (44 percent) and drastic when combined with joint slop (75 percent). The magnitudes will be mitigated to some extent when iterated The combined effects yield a tolerance contour close to the measuring tolerance for thrust misalignment. Upon this basis large flight motion disturbances and possible roll lock-in would be expected.

Comparison of predicted dynamic motion behavior with observed behavior for Flight 4.81 is presented in Fig. 9. The flight data, extracted from Ref. 25, exhibits dramatic change in roll rate and pitch frequency with roll lock-in occurring after 40 sec. Ref. 25 indicated the nose cone separation or structural failure may have caused the increasing pitch frequency.

The predicted rigid body motions exhibit breakout from roll resonance in the vicinity of 43 sec for large asymmetries. With the induced roll moment data of Ref. 26, severe lock-in was encountered for any asymmetry magnitude as shown by the curve labeled $C_{l_I} \times 10$. These C_{l_I} data were scaled down by a factor of ten for this simulation.

When the equivalent bending and joint aerodynamics are introduced at nominal resonance, the characteristic of the observed flight motion is fairly well simulated.

These curves clearly indicate the role of joint slop and body bending in aggravating the vehicle response to mass, aerodynamic and thrust asymmetries. It appears probable that the joint play is primary cause of the failures of the Aerobee 150 flights 4.81 and 4.86.

Section 3
ANALYSIS OF FIN FLEXIBILITY EFFECTS

3.1 SCOPE OF THE ANALYSIS

An analysis of fin flexibility was made with the principal aim of providing a general method for describing the total incremental effects of flexibility upon the aerodynamic characteristics of a vehicle composed of an elastic body and a number of elastic fins. The analysis is applicable to any number of fins or elastic appendages.

3.2 METHOD OF APPROACH

In the analysis which follows, attention is first directed towards investigating three fundamental methods for describing the structural properties of the fins alone. Since, in a condition of roll-resonance, the aerodynamic loads may be considered steady-state as opposed to flutter-type loads, stiffness of the fins is of principal interest. Three methods were investigated; namely, (1) a finite element description of fin stiffness, (2) an elastic axis concept for the fin for which the elastic motion is defined by bending and torsion and (3) a torque-box concept. Of the three methods, the torque-box concept was selected as the most useful for application to the Aerobee 150 or vehicles of similar fin geometry and construction.

Having defined the fin stiffness alone, attention is next directed towards writing the equations of motion of the flexible body and the equations of motion of the fins in aerodynamic proximity but structurally unrestrained by each other. Structural restraints require the introduction of a relative motion coordinate, μ, between fin and body which must vanish. The resulting equations of motion are then rewritten to satisfy dynamic equilibrium by invoking the Principle of Virtual Work. The set of equations obtained in this manner is partitioned in order to eliminate all elastic degrees of freedom. The final equations are of the same form previously obtained for a flexible body with rigid fins as described in Ref. 6.

3.3 ANALYSIS OF FIN STIFFNESS METHODS

3.3.1 Finite Element Approach

The most accurate description of fin stiffness, of the three methods studied, results from a finite element approach where a network of intersecting straight lines are taken to lie along the ribs and spars of the actual fin construction. For the Aerobee 150, the method was found to be very cumbersome because of the number of degrees of freedoms if used in a study in which stiffness must be varied as a parameter. A detailed description of the method for obtaining a matrix of stiffness coefficients is contained in Ref. 27.

3.3.2 Elastic Modes for a Fin

The elasticity of a fin can be represented with fair accuracy in the steady-state by two elastic modes, one for twisting and one for bending. These modes can be assumed in forms which satisfy with acceptable accuracy the root and tip conditions, with approximately correct shapes between root and tip. By this means the elastic degrees of freedom are reduced from the order of twenty (as used in the finite element method applied to the Aerobee 150) to two. The modal values at nodes of the finite-element network are taken to be

$$|\hat{\delta}|^t = \left| X\left(\frac{Y}{S}\right) - \frac{1}{2} X\left(\frac{Y}{S}\right)^2 \right| \quad \text{(twisting)}$$

$$|\hat{\delta}|^b = \left| \left(\frac{Y}{S}\right)^2 - \frac{2}{3}\left(\frac{Y}{S}\right)^3 + \frac{1}{6}\left(\frac{Y}{S}\right)^4 \right| \quad \text{(bending)}$$

where S is the span measured in the Y-direction as shown in Fig. 10.

Thus, the expression

$$\left[\{\epsilon\}\right]_F^F \left[[K]\right]_F^F \left[|\hat{\epsilon}|\right]_F^F \left|\lambda\right|_F$$

which appears in the expression for generalized elastic force (see the expression for the matrix quantity [E], in Fig. 6) becomes under the bending/torsion approach

$$\begin{bmatrix} \{\hat{\delta}\}_t \\ \{\hat{\delta}\}_b \end{bmatrix} \overset{*}{[K]} \left[|\hat{\delta}|^t \ , \ |\hat{\delta}|^b\right] \begin{vmatrix} \lambda_t \\ \lambda_b \end{vmatrix} = \begin{bmatrix} \hat{K}_t^t \ , & \hat{K}_t^b \\ \hat{K}_b^t \ , & \hat{K}_b^b \end{bmatrix} \begin{vmatrix} \lambda_t \\ \lambda_b \end{vmatrix}$$

The modes and generalized stiffnesses just described may be employed to locate the elastic axis depicted in Fig. 10. By definition, the elastic axis pierces a cross-section at the point where a load P must be applied in order to produce only translation of the section without rotation. The elastic axis connects all such cross-sectional points. If the elastic axis is straight or nearly so, it can be used in a transformation of coordinates that decouples twisting from bending. This is convenient in visualizing the angles of attack induced by aerodynamic loading. Location of the elastic axis is determined as follows: If a load P is applied at an arbitrary point X_P in a cross-section $Y = Y_P$, the deflection of the entire fin is given by

$$\begin{bmatrix} K_t^t \ , & \hat{K}_t^b \\ K_b^t \ , & \hat{K}_b^b \end{bmatrix} \begin{vmatrix} \lambda_t \\ \lambda_b \end{vmatrix} = P \begin{vmatrix} \hat{\delta}_P^t \\ \hat{\delta}_P^b \end{vmatrix}$$

where

$$\left[\delta_p^t = X_P\left(\frac{Y_P}{S}\right)\right] - \frac{1}{2}X_P\left(\frac{Y_P}{S}\right)^2$$

$$\hat{\delta}_P^b = \left(\frac{Y_P}{S}\right)^2 - \frac{2}{3}\left(\frac{Y_P}{S}\right)^3 + \frac{1}{6}\left(\frac{Y_P}{S}\right)^4$$

The value of X_P for which $\lambda_t = 0$ (no twisting) is the elastic-axis location X_{EA} for the cross-section. Thus, X_{EA} is given by

$$\begin{vmatrix} \hat{K}_t^b \\ \\ \hat{K}_b^b \end{vmatrix} \quad \lambda_b = P \begin{vmatrix} X_{EA}\left(\frac{Y_P}{S}\right) - \frac{1}{2}X_{EA}\left(\frac{Y_P}{S}\right)^2 \\ \\ \left(\frac{Y_P}{S}\right)^2 - \frac{2}{3}\left(\frac{Y_P}{S}\right)^3 + \frac{1}{6}\left(\frac{Y_P}{S}\right)^4 \end{vmatrix}$$

that is,

$$X_{EA} = \frac{\left(\frac{Y_P}{S}\right)^2 - \frac{2}{3}\left(\frac{Y_P}{S}\right)^3 + \frac{1}{6}\left(\frac{Y_P}{S}\right)^4}{\frac{Y_P}{S} - \frac{1}{2}\left(\frac{Y_P}{S}\right)^2} \frac{\hat{K}_t^b}{\hat{K}_b^b}$$

On this basis, the elastic axis is almost straight, having coordinates as follows:

Y_P/S	$X_{EA}\Big/\frac{\hat{K}_t^b}{\hat{K}_b^b}$
0	0
1/4	$\frac{27}{28} \times \frac{1}{4}$
1/2	$\frac{17}{18} \times \frac{1}{2}$
3/4	$\frac{19}{20} \times \frac{3}{4}$
1	1

It is seen that the elastic axis location is proportional to the ratio $\hat{K}_t^b / \hat{K}_b^b$, the location at the tip being

$$\left(X_{EA}\right)_{TIP} = \hat{K}_t^b \Big/ \hat{K}_b^b$$

The relative location of the aerodynamic center of pressure and the elastic axis is the primary index of the steady-state aeroelastic stability of a fin (stability is obtained for elastic axis forward of center of pressure). Thus, the influence of the fins' own stability on the overall vehicle performance may be studied simply by varying $\hat{K}_t^b = \hat{K}_b^t$ to reflect various elastic axis locations.

3.3.3 Fin Stiffness Represented as a Torque Box

The torque box-beam approach described here is cruder than that of the finite element method, reference Sec. 3.3.1, but the results can be stated more simply and are satisfactory for obtaining nominal generalized stiffness values about which parameters may be varied in a study of stiffness effects.

The fin is considered to be a cantilever beam, having bending and twisting cross-sectional rigidities EI and GJ which vary with the span wise coordinate. The elastic modulii E and G are assumed to be constant over the fin. The factors I and J are assumed to vary according to

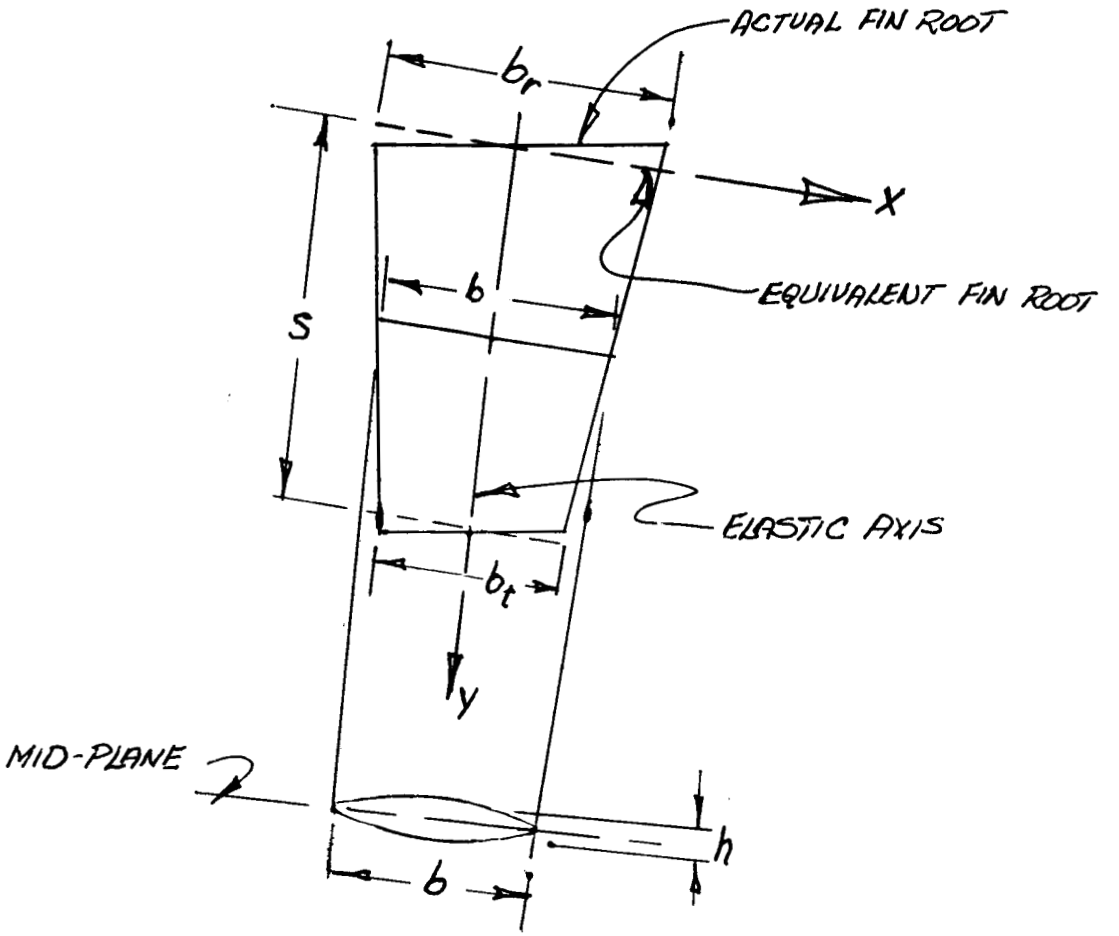

$$I = I_r \frac{bh^2}{b_r h_r^2} \quad ; \quad J = J_r \frac{bh^2}{b_r h_r^2}$$

where r designates values at the root. This law of variation is a good approximation for skin thickness constant over the fin and h/b ratios small or constant.

An XYZ axis system is placed as shown in the sketch, the X-Y plane being the mid-plane for bending, the Y-axis being the assumed or known position of a straight elastic axis. This axis system is skewed relative to body coordinates by the amount of sweep of the fin. Displacements are described by two assumed modes having the same forms as in Sec. 3.3.2 but related to the present axes, namely,

$$\hat{\tau} = \frac{Y}{S} - \frac{1}{2}\left(\frac{Y}{S}\right)^2 \qquad \text{(rotation about Y)}$$

$$\hat{\delta} = \left(\frac{Y}{S}\right)^2 - \frac{2}{3}\left(\frac{Y}{S}\right)^3 + \frac{1}{6}\left(\frac{Y}{S}\right)^4 \qquad \text{(translation in Z-direction)}$$

By definition, these modes are elastically uncoupled. The generalized stiffness are given by

$$\hat{K}_t^t = G\int_0^S J\left(\frac{d\hat{\tau}}{dY}\right)^2 dY$$

$$\hat{K}_b^b = E\int_0^S I\left(\frac{d^2\hat{\delta}}{dY^2}\right)^2 dY$$

These integrals work out to be

$$\hat{K}_t^t = \frac{1}{3}\left(1 - \frac{P}{4} + \frac{Q}{10} - \frac{R}{20}\right)\frac{GJ_r}{S}$$

$$\hat{K}_b^b = \frac{4}{5}\left(1 - \frac{P}{6} + \frac{Q}{21} - \frac{R}{56}\right)\frac{EI}{S^3}$$

where:

$$P = R_b + 2R_h \qquad R_b = 1 - \frac{b_t}{b_r}$$

$$Q = 2R_b R_h + R_h^2$$

$$R = R_b R_h^2 \qquad R_h = 1 - \frac{h_t}{h_r}$$

Generalized elastic forces are again expressed (as in Sec. 3.3.2) by

$$\begin{bmatrix} \{\hat{\delta}\}_t \\ \{\hat{\delta}\}_b \end{bmatrix} \left[\overset{*}{K}\right]_P^{\delta} \left[\left|\hat{\delta}\right|^t , \left|\hat{\delta}\right|^b\right] \cong \begin{bmatrix} \hat{K}_t^t & \\ & \hat{K}_b^b \end{bmatrix}$$

where $\hat{K}_t^t$ and $\hat{K}_b^b$ are given by the formulas above Arbitrary shifts of the elastic axis are represented by arbitrary changes in the coupling stiffness, in this case by insertion of coupling stiffness values to give

$$\begin{bmatrix} \hat{K}_t^t & \hat{K}_t^b \\ \hat{K}_b^t , & \hat{K}_b^b \end{bmatrix}$$

as the stiffness matrix, where

$$\hat{K}_t^b = \hat{K}_b^t = \hat{K}_b^b \left(X_{EA}\right)_{TIP}$$

X_{EA} is shown in Fig. 10.

The bending rigidity factor I is computed in the familiar way as the second moment of cross-sectional area about the mid-plane. The torsional factor J is computed for a cross-section of a general fin form sketched below as follows:

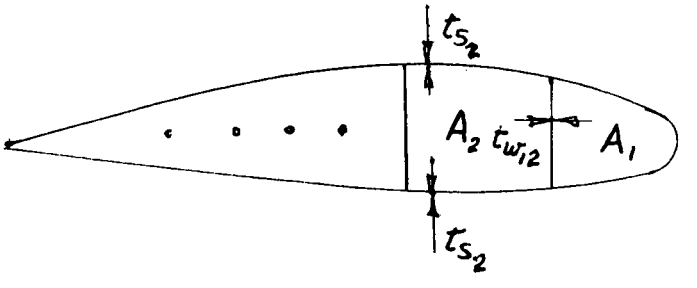

G assumed constant over section

t_s , skin thickness assumed constant over cell

t_w , web thickness assumed constant over web

A_i = area of cell i

t_{s_i} = thickness of skin over cell i

$t_{w_{ii}}$ = thickness of web between cells i and j

Let:

S_{s_i} = perimeter of skin over cell i

$S_{w_{ii}}$ = perimeter of web between cells i and j

$$S_i = \left(\frac{S_w}{t_w}\right)_{ii} + \left(\frac{S_s}{t_s}\right)_i + \left(\frac{S_w}{t_w}\right)_{jk}$$

$$S_{ii} = \left(\frac{S_w}{t_w}\right)_{ii}$$

Torsion theory for thin-walled tubes gives

$$J = 4\{A\}[S]^{-1}|A|$$

where $\{A\} = \{A_1, A_2, A_3, \ldots\}$

$$[S] = \begin{bmatrix} S_1 & -S_{12} & & \\ -S_{12} & S_2 & -S_{23} & \\ & -S_{23} & S_3 & -S_{34} \\ & & \cdot & \\ & & & \cdot \\ & & & & \cdot \end{bmatrix}$$

For the three-cell symmetric cross-section in Fig. 10

$$\{A\} = \{A_1 , A_2 , A_3\}$$

$$[S] = \begin{bmatrix} S_1 & -S_{12} & \\ -S_{12} & S_2 & -S_{12} \\ & -S_{12} & S_1 \end{bmatrix}$$

$$J = 4 \frac{2S_2 A_1^2 + 4S_{12} A_1 A_2 + S_1 A_2^2}{S_1 S_2 - 2S_{12}^2}$$

Having obtained fin stiffness by this method, we may proceed to follow the steps shown in Fig. 10 which are described in detail in Section 3.4 and 3.5.

3.4 UNCOUPLED BODY/FIN DYNAMICS

The motion dynamics of each subsystem, such as a single fin, are first described with respect to its own reference axes. The equations of motion for all particles of that subsystem will have the form presented in Fig. 4 but with an additional coordinate included. This generalized relative coordinate μ describes the position and orientation of the subsystem reference axes with respect to the reference axes of the complete vehicle. The complete equations for all subsystems in aerodynamic proximity but with structural isolation may then be written as:

3.1

$$\begin{bmatrix} [A]^{B}_{B} & [A]^{F_1}_{B} & \cdots \\ [A]^{B}_{F_1} & [A]^{F_1}_{F_1} & \cdots \\ \cdot & \cdot & [A]^{j}_{i} \\ \cdot & \cdot & \\ \cdot & \cdot & \end{bmatrix} \begin{Vmatrix} \\ |\tau| \\ \\ |\lambda| \\ \\ |\tau| \\ \\ |\mu| \\ \\ |\lambda| \\ \\ \cdot \\ \cdot \end{Vmatrix}_{B} \Bigg|_{F_1} = \begin{vmatrix} [B]^{B}_{B} + [B]^{F_1}_{B} + \cdots \\ [B]^{B}_{F_1} + [B]^{F_1}_{F_1} + \cdots \\ \cdot \quad \cdot \quad \cdot \\ \cdot \quad \cdot \quad \cdot \\ \cdot \quad \cdot \quad \cdot \end{vmatrix}$$

where the subscripts and superscripts designate:

B = body without fins

F_1, F_2, F_3, ... = fins numbered 1, 2, 3, ...

The coordinates are now defined by:

$$|\tau|_i = \begin{Vmatrix} |\bar{v}| \\ \\ |\omega| \end{Vmatrix}_i = \text{rigid body velocities and angular rates}$$

$|\lambda|_i$ = generalized coordinates of elastic displacements

$|\mu|_i$ = generalized coordinates of relative rigid-body displacements for each i^{th} subsystem.

The element matrices represents the 3×3 coefficient array

$$[A]_i^j = \begin{bmatrix} [A]_\tau^\tau , & [A]_\tau^\mu , & [A]_\tau^\lambda \\ [A]_\mu^\tau , & [A]_\mu^\mu , & [A]_\mu^\lambda \\ [A]_\lambda^\tau , & [A]_\lambda^\mu , & [A]_\mu^\mu \end{bmatrix}_i^j$$

and the column coefficient array

$$[B]_i^j = \begin{vmatrix} |B|_\tau \\ |B|_\mu \\ |B|_\lambda \end{vmatrix}_i^j$$

The individual coefficients are defined as follows:

$$[A]_{\tau_i}^{\tau_j}$$

$$= [A]_{\mu_i}^{\tau_j} = -\begin{bmatrix}\{[1]\}\\ \{[d_o]'\}\end{bmatrix}_i^i \left[\left|[\omega]\right|_i^j \left|[m]\right|_j^j + \frac{1}{\bar{u}_j}\left[[\ell]\right]_i^j \left|[1]\right|_i^j \;,\; \left|[\omega]\right|_i^j \left|[\sigma_o]\right|_j^j + \frac{1}{\bar{u}_j}\left[[\ell]\right]_i^j \left|[d_o]\right|_j^j - 2\left|[h_o]\right|_i^j\right]$$

$$[A]_{\mu_i}^{\tau_i}$$

$$= -\left[\{\hat{\epsilon}\}\right]_i^i \left[\left|[\omega]\right|_i^j \left|[m]\right|_j^j + \frac{1}{\bar{u}_j}\left[[\ell]\right]_i^j \left|[1]\right|_j^j \;,\; \left|[\omega]\right|_i^j \left|[\sigma_o]\right|_j^j + \frac{1}{\bar{u}_j}\left[[\ell]\right]_i^j \left|[d_o]\right|_j^j - 2\left|[h_o]\right|_i^j\right]$$

$$[A]_{\tau_i}^{\mu_j} =$$

$$= [A]_{\mu_i}^{\mu_j} = \begin{bmatrix}\{[1]\}\\ \{[d_o]'\}\end{bmatrix}_i^i \left[\left[\left|[\omega]^2\right|_i^j \left|[m]\right|_j^j + \frac{1}{\bar{u}_j}\left[[\ell]\right]_i^j \left|[\omega]\right|_j^j\right]\left[\left|[1]\right| \;,\; \left|[d_o]\right|\right]_j^j + \left[[\ell]\right]_i^j \left[\left|[0]\right| \;,\; \left|[\textcircled{1}]\right|\right]_j^j\right]$$

$$[A]^{\mu_j}_{\lambda_i}$$

$$= \left[\{\hat{\epsilon}\}\right]^i_i \left[\left[\left[[\omega]^2\right]^j_i \left|\lceil m \rfloor\right|^j_j + \frac{1}{\bar{u}_j}\left[[\ell]\right]^j_i \left[[\omega]\right]^j_j\right]\left[\left|\lceil 1 \rfloor\right| \ , \ \left|[d_o]\right|\right]^j_j + \left[[\ell]\right]^j_i \left[\left|[0]\right| \ , \ \left|[\textcircled{1}]\right|\right]^j_j\right]$$

$$[A]^{\lambda_j}_{\tau_i} =$$

$$[A]^{\lambda_j}_{\mu_i} = \left[\begin{matrix}\{\lceil 1 \rfloor\} \\ \{[d_o]'\}\end{matrix}\right]^i_i \left[\left[\left[[\omega]^2\right]^j_i \left[\lceil m \rfloor\right]^j_j + \frac{1}{\bar{u}_j}\left[[\ell]\right]^j_i \left[[\omega]\right]^j_j\right]\left[\left|\hat{\epsilon}\right|\right]^j_j - \left[\left|[p_o]\right|^j_i + 2\left[[\omega]\right]^j_i [h_o]^j_j\right]\left[|p_E|\right]^j_j + \left[[\ell]\right]^j_i \left[\left|\hat{\epsilon}'\right|\right]^j_j\right]$$

$$[A]_{\lambda_i}^{\lambda_j}$$

$$= \left[\{\hat{\epsilon}\}\right]_i^i \left[\left[\left[[\omega]^2\right]_i^j \left[\lceil m \rfloor\right]_j^j + \frac{1}{\bar{\mu}_j}\left[[\ell]\right]_i^j \left[[\omega]\right]_j^j + \left[[k]\right]_i^j\right]\left[|\hat{\epsilon}|\right]_j^j - \left[|[p_o]|_i^j + 2\left[[\omega]\right]_i^j |[h_o]|_j^j\right]\left[|\hat{\rho}_E|\right]_j^j + \left[[\ell]\right]_i^j\left[|\hat{\epsilon}'|\right]_j^j\right]$$

$$|B|_{\tau_i}^j = |B|_{\mu_i}^j = \begin{bmatrix}\{\lceil 1 \rfloor\} \\ \{[d_o]'\}\end{bmatrix}_i^i \left|\left||p_o|\right|_i^j + \left||\ell_o|\right|_i^j + |\lceil m \rfloor|_i^j |g|_j^j\right|$$

$$|B|_{\lambda_i}^j = \left[\{\hat{\epsilon}\}\right]_i^i \left|\left||p_o|\right|_i^j + \left||\ell_o|\right|_i^j + |\lceil m \rfloor|_i^j |g|_j^j\right|$$

The coefficient elements, such as the rotation matrix $[\omega]$, are defined in Ref. 6. The significance of the submatrices such as $[\ell]_i^j$ is extended from that in Ref. 6 to relate physical effects produced in one subsystem by an action of a point in another subsystem. For example,

$$\left[[\ell]\right]_F^B = \begin{bmatrix} [\ell]_a^a , & [\ell]_a^b , & \cdots \\ [\ell]_b^a , & [\ell]_b^b , & \cdots \\ \cdot & \cdot , & \cdots \\ \cdot & \cdot , & \cdots \end{bmatrix}_F^B$$

where $[\ell]_{aF}^{cB}$ represents the aerodynamic forces generated at point a in subsystem F by unit angles of attack at point C in system B.

3.5 STRUCTURAL RESTRAINTS

In order to construct the force and moment balance of Eq. (3.1) for the complete vehicle from the isolated subsystem descriptions, the geometric and structural constrints are prescribed by

$$
(3.2)\quad
\begin{vmatrix}
\begin{vmatrix} |\tau| \\ |\lambda| \end{vmatrix}_B \\
\\
\begin{vmatrix} |\tau| \\ |\mu| \\ |\lambda| \end{vmatrix}_{F_1} \\
\cdot \\
\cdot
\end{vmatrix}
=
\begin{bmatrix}
[1]^{\tau B}_{\tau B} & & & & & & \\
& [1]^{\lambda B}_{\lambda B} & & & & & \\
[R]^{\tau B}_{\tau F1} & & & & & & \\
& [R]^{\lambda B}_{\mu F1} & [R]^{\lambda F1}_{\mu F1} & \cdot & & & \\
& & [1]^{\lambda F1}_{\mu F1} & & \cdot & & \\
\cdot & \cdot & \cdot & \cdot & \cdot & \cdot & \cdot \\
\cdot & \cdot & \cdot & \cdot & \cdot & \cdot & \cdot
\end{bmatrix}
\begin{vmatrix}
|\tau|_B \\
|\lambda|_B \\
|\lambda|_{F1} \\
|\lambda|_{F2} \\
\cdot \\
\cdot \\
\cdot
\end{vmatrix}
$$

where for example $[R]^{\tau B}_{\tau F1}$ represents the position and orientation transformation between the F1 subsystem reference axes and the B system reference axes.

Hence the coordinates of the Fi subsystem with respect to the B system are given by

$$|\tau|_{Fi} = [R]^{\tau B}_{\tau Fi} |\tau|_B$$

where

$$[R]^{\tau B}_{\tau Fi} = \begin{bmatrix} [C]^{fB}_{fFi} , & [C]^{fB}_{fFi}\,[\Delta Fi]^{fB}_{fB} \\ [O]^{fB}_{fFi} , & [C]^{fB}_{fFi} \end{bmatrix}$$

$[C]^{fB}_{fFi}$ represents the direction cosine matrix between the Fi and B reference axes and

$$[\Delta]^{fB}_{fB} = \begin{bmatrix} & \overline{Z}Fi , & -\overline{Y}Fi \\ -\overline{Z}Fi & & \overline{X}Fi \\ \overline{Y}Fi , & -\overline{X}Fi & \end{bmatrix}^{fB}_{fB}$$

the relative displacement of the reference axes origins.

The relation between the relative rigid body coordinates μ and the elastic coordinates λ is given by the terms

$$[R]^{\lambda B}_{\mu Fi} = \begin{bmatrix} [C]^{fB}_{fFi} & \\ & [C]^{fB}_{fFi} \end{bmatrix} \begin{bmatrix} |\hat{\epsilon}| \\ |\hat{\rho}| \end{bmatrix}_{B\ \rho\ Fi\ \rho\ R}$$

and

$$[R]^{\lambda Fi}_{\mu Fi} = -\begin{bmatrix} |\epsilon| \\ |\rho| \end{bmatrix}^{Fi}_{Fi\ ,\ B\ ,\ R}$$

where $\hat{\epsilon}$ and $\hat{\rho}$ are the elastic modal displacement and rotations, respectively. The subscript (B , Fi , R) denotes B system values at the point of its junction with system Fi and similarly for subscript (Fi , B , R).

3.6 EQATIONS OF MOTION WITH STRUCTURAL RESTRAINTS

The structural restraints described above are now applied to the Eq. 3.1 to account for the relative coordinate μ after which the principal of virtual work is applied to eliminate the elastic coordinate λ. The structurally unrestrained equations (Eq. 3.1) may be written as

$$[A] \; |q| = |B|$$

Applying the structural restraints (Eq. 3.2) yields the coordinates q in terms of the isolated coordinate τ and λ as

$$|q| = \left[[R]^{\tau B} , [R]^{\lambda} \right] \begin{vmatrix} |\tau|_B \\ |\lambda| \end{vmatrix}$$

and Eq. 3.1 becomes

$$\begin{bmatrix} [R] \\ \quad {}^{\tau B} \\ [R]_{\lambda} \end{bmatrix} [A] \left[[R]^{\tau B} , [R]^{\lambda} \right] \begin{vmatrix} |\tau|_B \\ |\lambda| \end{vmatrix} = \begin{bmatrix} [R]_{\tau B} \\ \\ [R]_{\lambda} \end{bmatrix} B \tag{3.3}$$

where

$$[R]_{\tau B} = \left[[R]^{\tau B} \right]'$$

and

$$[R]_{\lambda} = \left[[R]^{\lambda} \right]'$$

are the transposed constraint matrices.

The restrained equation (3.3) when condensed to

$$\begin{bmatrix} [\overset{*}{A}]^{\tau B}_{\tau B} & , & [\overset{*}{A}]^{\lambda}_{\tau B} \\ [\overset{*}{A}]^{\tau B}_{\lambda} & , & [\overset{*}{A}]^{\lambda}_{\lambda} \end{bmatrix} \begin{vmatrix} |\tau|_B \\ |\lambda| \end{vmatrix} = \begin{vmatrix} |\overset{*}{B}|_{\tau B} \\ |\overset{*}{B}|_{\lambda} \end{vmatrix} \tag{3.4}$$

where typically

$$[A]^{\tau B}_{\tau B} = [R]_{\tau B} [A] [R]^{\tau B}$$

are reduced to the form of the body alone equations of Ref. 6.

From this point the development proceeds exactly as in Ref. 6 to yield the equations of Fig. 11. Direct comparison with the final equation of Fig. 6 will clarify the new notation used for the more comprehensive treatment. The equations are again divided into the rigid vehicle elements and the aero elastic corrections for the steady state roll resonance condition.

3.7 SUMMARY COMMENT ON FIN FLEXIBILITY

Of the three methods investigated for representing fin flexibility, the torque box-beam concept appears to offer the most convenient method for investigating stiffness parameters in conventional spar-ribfin construction and is recommended for this purpose. In the case of slab fins, the elastic-axis concept is recommended.

The method for formulating the equations of motion presented is applicable to any vehicle containing elastic elements which may be conveniently studied as sub-systems. As a practical matter, the method is most useful when used in connection with a digital computer because of the large numbers of degrees of freedom which must be handled. No attempt has been made to mechanize the equations of the present section on a computer since this effort was beyond the scope of the contract. However, such mechanization appears to be easily attained from a modification to the present FLEXCOR program.

Section 4
RIGID BODY ROLL RESONANCE WITH BODY-FIN FLOW INTERACTION

The previous analyses of Ref. 1, 2, 4, 5, and 6 demonstrated roll lock-in phenomena for symmetrical linear aerodynamics except for non-linear induced roll moments. While the existence of side forces and pitch/yaw moments due to the same source as the induced roll moment were recognized, they are not essential to the basic mechanism causing roll lock-in. The magnitudes are relatively small and act in a destabilizing mode to degrade the tolerance to roll resonance. Since the flow interaction characteristics are highly non-linear in angle of attack and side slip, analytical solutions are not readily available and resort to numerical evaluation is required. In the same sense, symmetrical non-linear characteristics were neglected at small angles of attack and at large angles were assumed to degrade the roll lock-in asymmetry tolerances. Again analytical solution for non-linear characteristics are severely limited and numerical evaluation is required for definitive assessment of such effects.

Refinements of the basic theory and procedures to incorporate these "real life" effects are described in this section.

4.1 Review of Flow Interaction Phenomena

The aerodynamic characteristics of body fin combinations have been studied extensive (Refs. 10-18). A flow visualization and generally accepted correlation parameters are summarized in Fig. 12 for a representative sounding rocket configuration. The normal force characteristics of the fins in the presence of the body can be described analytically in terms of the carryover factor K_w and the isolated fin derivative C_{N_α}. In similar manner, the effect of leading edge sweepback is described in terms of the parameter K_ϕ, the sweepback angle ϵ, side slip angle, and the isolated fin derivative. The influence of vortex flow generated by body cross flow is not as easily characterized.

The asymmetric location of the vortices at combined angle of attack and side slip yield differential loading on each fin producing a net rolling moment and resultant forces and moments not in the plane of resultant angle of attack. Spahr has shown that with known positions of the vortices, the loading can be predicted quite closely as shown in Fig. 13. The theory predicts the measured data well for a representative four fin configuration. The effect of the vortices is sufficient to completely unload the upper fin at small β while the effect on the lower fin is minor. The length of the forebody exerts a significant influence also as depicted by the lower curves. The longer forebody appears to either provide a stronger vortex and more asymmetric orientation (or both) causing greater unloading of the fin. The longitudinal location of vortex shedding was found to be principal uncertainty inhibiting accurate prediction of vortex effects. In order to provide definitive numerical evaluation of induced forces and moments from this source, resort to wind tunnel data appears necessary for a particular sounding rocket configuration.

4.2 Description of the Aerodynamic Characteristics

The induced roll moment is described as a function of the resultant angle of attack (α_T) and Mach number (M) plus a sinusoidal variation with roll orientation (ϕ) of the angle of attack [i.e., $C_{\ell_I} = C_{\ell_I}(\alpha_T, M) \times \sin N\phi$ where N is the number of fins]. This formulation was found to represent the measured characteristics (Refs. 1−6) adequately for determination of roll lock-in tolerances and demonstration of the roll resonance phenomena.

The flow induced side forces and moments exhibit characteristics similar to the induced rolling moment, i.e., highly non-linear with angle of attack and roll orientation (Ref. 19−20). Furthermore, the symmetrical pitch force and moment characteristics exhibit considerable non-linearity in the angle of attack region of interest. Since the induced characteristics would introduce non-linear terms into the existing equations of motion and the equilibrium solutions, it was decided to provide for

non-linearity in all of the aerodynamic characteristics. The force and moment coefficients then take the form:

$$C_X = C_X(\alpha_T, M) + C_{X_1}(\alpha_T, M) \sin \frac{N}{2} \phi$$

$$C_Y = C_Y(\beta, M) + C_{Y_1}(\alpha_T, M) \sin N\phi$$

$$C_N = C_N(\alpha, M) + C_{N_1}(\alpha_T, M) \sin \frac{N}{2} \phi$$

$$C_\ell = C_{\ell_1}(\alpha_T, M) \sin N\phi$$

$$C_m = C_m(\alpha, M) + C_{m_1}(\alpha_T, M) \sin \frac{N}{2} \phi$$

$$C_n = C_n(\beta, M) + C_{n_1}(\alpha_T, M) \sin N\phi$$

Typical aerodynamic characteristics for the Aerobee 350 vehicle (Ref. 20) are depicted schematically in Fig. 14 with the above formulation. Note that the induced pitching moment, normal force, and axial force exhibit a sin 2ϕ variation while the induced roll moment, yawing moment, and side force follow a sin 4ϕ variation. The basic symmetry of the sounding rocket is retained in the principal force and moment terms (e.g., $C_{m_i} = C_{n_i}$). The degree of non-linearity with angle of attack in the coefficients is indicated by comparison with the slopes at zero angle of attack which were used in previous studies. The pitching moment exhibits a decreasing slope ("softening") up to about $\alpha = 8$ deg after which it becomes unstable. Between M = 4 and M = 5, the unstable slope disappears and an increasing ("hardening") slope become evident. Although different payload weight and length will change the magnitude, the coefficients depicted here will serve to illustrate the effects of a wide range of non-linear characteristics.

4.3 Equations of Motion With Induced and Non-Linear Aerodynamic Characteristics

The body-fixed equations of motion (refs. 1,2,4) require modification of the coefficients as illustrated in Fig. 15. Separate coefficients are now identified with the pitch and yaw equations. For example, A11 and A12 were formally described by a single A1 in terms of the rotationally symmetry aerodynamic derivatives. The linearized derivatives C_{m_α} and C_{n_β} are replaced with average slopes C_m/α and C_n/β. The damping derivatives are defined as the local slopes [e.g., C_{N_α} is replaced by $(\partial C_N/\partial\alpha)_\alpha$] . The small angle approximation is retained and motion described with respect to the principal axis.

The modifications to the dynamic motion option of the RPM Program are summarized in Appendix I. A double table look-up in angle of attack and Mach number for aerodynamic coefficient magnitude and slope is utilized. Non-linear and induced aerodynamic characteristics are stored in separate tables to account for the orientation effect on induced coefficients. The terms involving the B_{ij} coefficients are mechanized differently than depicted in Fig. 10 to avoid singularities at zero α on β. The magnitude of the appropriate aerodynamic term (e.g., $C_m\bar{q}Ad/I$) rather than its derivative (e.g., $C_{m_\alpha}\bar{q}Ad/I$) is computed. The integration procedures remain unchanged.

4.4 Equilibrium Roll Resonance Response

The non-linear character of the flow induced side forces and moments requires a new procedure for the calculation of the center of gravity tolerance for lock-in. With the linearized aerodynamic characteristics, the peak angle of attack is uniquely defined throughout the trajectory because resonance occurs at a specific roll rate equal to the aerodynamic pitch frequency. For a non-linear pitching moment characteristic, this frequency is dependent upon the magnitude of the angle of attack. Hence, the rolling trim response is altered from the linear case as illustrated in Fig. 16 for the softening pitching moment coefficient illustrated in Fig. 14. (The aerodynamic frequency ω is defined by the zero angle-of-attack pitching moment derivative in both cases.) The

principal effect of interest here is to move the peak resonant angle of attack from point A at $p/\omega = 1$ for the linear case to point B at $p/\omega < 1$ for the non-linear case.

The peak amplification increases due to the decrease in the effective aerodynamic damping resulting from the induced side force and moments.

The phase shift ϕ is essentially -90 deg at resonance in either case. Therefore, the arrangement of asymmetries yielding the largest roll torque and the smallest magnitude of center of gravity offset required for roll resonance is unchanged from the linear case as is shown in the right-hand side of Fig. 16.

This basic understanding and description of motion behavior was developed by Kanno (Ref. 23) for ballistic reentry vehicles with non-linear aerodynamic characteristics. The approach used here represents an extension of this analysis to sounding rockets.

4.5 Equilibruim Solution Procedure

The procedure for determining the peak angle of attack and spin rate at resonance (point B of Fig. 16) is summarized in Fig. 17.

The steady state portions of the equations of motion of Fig. 15 are manipulated first to extract the aerodynamic restoring moment and the gyroscopic moment and, secondly, to extract the damping moment and the asymmetry moment. The spin rate is calculated as a function of angle of attack for two conditions: (1) the gyroscopic moment balances the aerodynamic restoring movement (p_1) and (2) the damping moment balances the asymmetry moment (p_2). The functions p_1 and p_2 are then interpolated to obtain the α_p and p at roll resonance. The method is depicted in the sketch on Fig. 17.

The expressions for spin rate in Fig. 17 were simplified by neglecting the difference in the induced lift terms in p_1 and by neglecting the induced moment difference in p_2.

The numerical computation procedure selected for the RPM program utilizes a trial solution technique. The calculations are started at a small finite angle of attack (α_T of Fig. 17) to avoid the singularity at zero α. The angle of attack is then incremented until p_1 exceeds p_2 or the preset maximum angle of attack is exceeded. The accuracy of the interpolated value is controlled primarily by selection of the α_T increment size.

The interpolated angle of attack α_P and spin rate p corresponding to point B of Fig. 16 are used to calculate the c.g. offset required to maintain this resonant condition. The procedure is then repeated for the next time point and trajectory condition. Hence, the straight forward determination of the c.g. offset for resonance feature of the linear solution is retained. The additional computations at each time point result in a six fold increase in run time (7 time points per second).

A comparison of the c.g. tolerance histories with linear, induced, and non-linear aerodynamics is presented in Fig. 18. The curves for various orientations Γ intersect at a common point for the linear case. This intersection yields the c.g. tolerance for trim asymmetry under consideration. The induced aerodynamics are seen to yield two intersections due to the change of the aerodynamic damping. The lower intersection again sets the c.g. tolerance. The change from the linear case is slight for the C_{m_o} illustrated. The cases for thrust misalignment exhibit the same characteristics.

The asymmetry tolerance contours derived by this procedure are presented in Fig. 19. The contours for linear aerodynamics from ref. 4 matched with the new formulation in the RPM program as indicated by the small circles on the solid lines. Flexibility produces only a minor reduction in the contour for the aerodynamic asymmetry. The induced aerodynamics produce a more significant effect due to the reduction in effective aerodynamic damping. For thrust misalignment, the corresponding effects are reversed. Since the intercept value is reduced by 12% for ϵ, the induced and non-linear effects are not expected to affect the Aerobee 350 dynamic performance significantly.

These contours were tested with dynamic motion runs on the modified RPM. As shown by the open and closed symbols at $\Delta CG = 1.0$ and 0.0 in. The contours based on equilibrium criteria remain conservative.

The effects of the induced and nonlinear aerodynamics on the dynamic behavior is illustrated in Fig. 20. At a zero ΔCG the motion departs from the linear behavior considerably due to the larger angles of attack resulting from the reduced aerodynamic damping. The roll rate experiences significantly larger excursion for both the induced and non-linear characteristics. The angle of attack locus exhibits similar excursions as denoted by the inside loops occurring above resonance. The case with induced plus linear terms demonstrates the classic roll lock-in behavior. The nonlinear case demonstrates the conservatism inherent in the equilibrium solution. The trim asymmetry used for this case is on the contour whereas the same value is beyond the corresponding contour with the induced terms.

Thus the general character of the vehicle motion is unchanged with the introduction of non-linear and induced aerodynamics. The procedure for evaluating allowable preflight asymmetry tolerances differs from that for linear aerodynamics in numerical computation method rather than in kind. Furthermore, the tolerance contours, based on steady state solutions are shown to be conservative to about the same degree.

Section 5
BODY-FIN FLOW INTERACTION WITH BODY BENDING

The preliminary investigation of the effects of body bending on induced fin loading was conducted primarily to determine the pertinent phenomena and to identify the critical parameters and incertainties. The general phenomena for the flow interactions of interest were discussed in Section 4 for the rigid body.

It was originally thought that the flexibility effects could be treated by assuming that the change in vortex location at the fins could be related directly to the nose deflection. Examination of the extensive experimental evidence for rigid bodies indicated that small changes in angle of attack do not radically change the location of the vortex at the fins. (Experimental data for bent bodies were not found.) This indicates that the vortices from the nose region tend to follow the body streamlines or that the body cross-flow immediately forward of the fins exerts a predominant effect.

These considerations led to the preliminary conclusions that only a second order effect on induced fin loading would result from body bending, and that prediction of the vortex location is the critical uncertainty. For the stiff fin designs used on the Aerobee 150, 150A,and 350 vehicles, the small change of loading does not warrant persuing the investigation further. For more flexible fins (such as the slab designs uses on Nike Apache), experimental data would be required to yield a difinitive evaluation.

Section 6
SUMMARY, CONCLUSIONS AND RECOMMENDATIONS

The influence of joint slop, body flexibility, induced and nonlinear aerodynamics upon sounding rocket roll resonance behavior has been demonstrated. A new computation tool (FLEXCOR) for examining multiple-jointed, body extensions has been developed which is applicable to sounding rockets in general. A method for accommodating fin flexibility in the FLEXCOR program has been formulated. The existing RPM program for rigid bodies has been suitably modified to accommodate non-linear and induced aerodynamics in both the dynamic and c.g. tolerance options. A brief preliminary examination of the effects of body bending on induced fin loading was conducted.

The following conclusions were drawn from the investigation described in the preceding sections:

- Joint rotation can provide a major source for roll lock-in
- Joint compliance and vehicle bending yield minor increase in aerodynamic trim asymmetry but a major increase of thrust misalignment.
- Fin flexibility effects on roll resonance behavior can be treated in a straight forward manner. The cost of mechanizing into FLEXCOR does not appear to be warranted for current fin design.
- Induced fin loading with rigid bodies are insufficiently predicted for determination of body bending effects.
- Induced side forces and moments cause significant but acceptable reduction in asymmetry tolerances

The development of methods and program accomplished during this study provide the necessary design tools for precise assessment of the effects of vehicle length, number of joints, payload weight for any sounding rocket. For example, maximum allowable length can now be evaluated for a given vehicle and flight condition with respect to roll

lock-in, maximum angle of attack or motion behavior during the test period. It is suggested that these methods be applied to current and development sounding rockets to establish a more difintive criterion for maximum vehicle length, fin-cant, maximum number of joints, payload weight and location.

Section 7
NEW TECHNOLOGY

One reportable item under the meaning of the New Technology Clause (ref. 21) was developed during the study. This item has been reported through the LMSC New Technology Representative (ref. 24) under the Title: "Elastic Corrections to Rigid Rocket Aerodynamic , Geometric and Thrust Asymmetries (FLEXCOR)."

Section 8

REFERENCES

1. D. A. Price, Jr. and E. O. Nelson, Final Report for the Aerobee 150A Roll Lock-In Study, Contract No. NAS 5-9061, Lockheed Missiles & Space Co., Sunnyvale, Calif., Feb 1965

2. D. R. McNeal, Description and Users Manual for Roll-Pitch Motion Digital Computer Program, LMSC Report No. M-60-64-2, Sunnyvale, Calif., Feb 1965

3. P. A. Sallow, Aerobee 350 Roll-Yaw Coupling Study, S.G.C. Report No. 379 RC-2, Space General Corporation, El Monte, Calif., Dec 1964

4. D. A. Price, Jr. and E. O. Nelson, Final Report for the Aerobee 350 Roll Lock-In Study, Extension to Contract No. NAS 5-9061, Lockheed Missiles & Space Co., Sunnyvale, Calif., Jun 1965

5. D. A. Price, Jr., E. O. Nelson, and J. E. Torrillo, Investigation of In-Flight Roll Control Techniques for Sounding Rockets, Contract No. NAS 5-9628, LMSC Report No. L-31-65-11, Sunnyvale, Calif., Dec 1965

6. D. A. Price, Jr. and P. S. Woods, Final Report on Roll Resonance Phenomena for Sounding Rockets, Contract No. NAS 5-10111, LMSC Report No. K-08-66-6, Sunnyvale, Calif., Dec 1966

7. R. Dotson, Description of Aeroelastic Corrections Program for Spinning Sounding Rockets, LMSC/685428, Sunnyvale, Calif., Apr, 1968

8. E. K. Maun, Development of a Roll Lock-In Criterion, S.G.C. Report No. 785 FR-3, Space General Corp., El Monte, Calif., Jul 1965

9. J. E. Brunk, Studies of the Near-Resonant Motion of Sounding Rocket Vehicles, ARI Report No. 65-2, Alpha Research, Inc., Santa Barbara, Calif., Jul 1965

10. J. Richard Spahr, Theoretical Investigation of the Effects of Configuration Changes on the Center-of-Pressure Shift of a Body-Wing-Tail Combination Due to Angle of Attack and Mach Number at Transonic and Supersonic Speeds, NACA TN 3966, May 1957

11. -----, Contribution of the Wing Panels to the Forces and Moments of Supersonic Wing-Body Combinations at Combined Angles, NACA TN 4146, Jan 1958

12. -----, Theoretical Prediction of the Effects of Vortex Flows on the Loading, Forces and Moments of Slender Aircraft, NASA TR R-101, 1961

13. John P. Gapcynski, An Experimental Investigation of the Flow Phenomena Over Bodies at High Angles of Attack at a Mach Number of 2.01, NACA RM L55H29

14. William C. Hayes, Jr. and Robert A. Kilgore, Transonic Wind-Tunnel Measurements of Some Dynamic Longitudinal and Directional Stability Parameters for a Finned Spinning Body of Revolution Having a High Fineness Ratio, NASA TM X-594

15. James C. Ferris, Static Stability Investigation of a Single-Stage Sounding Rocket at Mach Numbers from 0.60 to 1.20, NASA TN D-4013, Jun 1967

16. Donald C. Babb and Dennis E. Fuller, Static Stability Investigation of a Sounding-Rocket Vehicle at Mach Numbers from 1.50 to 4.63, NASA TN D-4014, Jun 1967

17. Leon H. Schindel, Separated Flow About Lifting Bodies, Massachusetts Institute of Technology, Aerophysics Lab, Technical Report 80

18. P. Kenneth Pierpont, Preliminary Investigation of Interference Effects of Multi-coplanar Fins on a Two-Stage Rocket Launch Vehicle With Winged Spacecraft at Transonic Speeds, NASA TM X-677

19. J. D. McNerney and D. L. Walker, Aerobee 350 Wind Tunnel Test Report, S.G.C. Report No. 379 RC-L, Space General Corp., El Monte, Calif., Aug 1964

20. J. D. McNerney, Aerobee 350 Wind Tunnel Test Analysis, S.G.C. Report No. 265 FR-8, Space General Corp., El Monte, Calif., Jan 1963

21. J. T. Lawrence, Aerobee 150A Aerodynamic Data From NOL Wind Tunnel Tests, GSFC Report No. X-671-64-47, NASA Goddard Space Flight Center, Greenbelt, Md., Feb 1964

22. J. T. Lawrence, Some Aspects of the Flight Dynamics of the Aerobee 350 in the Region of Pitch-Roll Coupling, GSFC Report No. X-671-65-252, NASA Goddard Space Flight Center, Greenbelt, Md., Jun 1965

23. J. S. Kanno, Spin Induced Forced Resonant Behavior of a Ballistic Body Having Stable Non-Linear Aerodynamic Properties, LMSC-48381; General Research in Flight Sciences, Jan 58 – Jan 59; Vol. IV, Jan 1959

24. NASA-NHB 2170.2, Reportable Items Under the New Technology Clause, Oct 1966

25. J. R. Busse, M. T. Leffler, G. E. Kraft, and P. S. Bushnell, Jr., A Compendium of NASA Aerobee Sounding Rocket Launchings for 1964, NASA TN D-3912, July 1967

26. W. Hatalsky, Vehicle Attitude Study Data Input for Six-Degrees of Freedom IBM 7090 Computer Program (Aerobee 150 with 150-Pound Payload and 27-inch Extension), Inter-Office Correspondence 5135:M0024, Space General Corp., 28 Mar 1963

27. M. L. Gossard, An Investigation of Three Methods for Stiffness Representation of a Fin, SS/1268/5522, 29 Feb 1967

Section 9

GLOSSARY

A	Reference area -ft^2
A_{ij}, B_{ij}, C_i	Coefficients in the equations of motion
a	Nozzle offset - in.
b	$R(\bar{q}A/mV)\left[C_{L_\alpha}(1 - Ix/I) - \frac{md^2}{I}\left(C_{m_q} + C_{n_{p\alpha}}\right)\right]$
C_A	Axial force coefficient
C_{A_I}	Induced axial force coefficient
C_L	Lift force coefficient
C_{L_I}	Induced lift force coefficient
C_{L_α}	Lift force coefficient derivative, 1/rad
C_ℓ	Roll moment coefficient
C_{ℓ_I}	Induced roll moment coefficient
C_{ℓ_δ}	Roll moment coefficient due to differential fin cant, δ, on each fin, 1/rad
C_{ℓ_p}	Roll damping coefficient based on pd/2V, 1/rad
C_m	Pitch moment coefficient
C_{m_I}	Induced pitch moment coefficient
C_{m_o}	Resultant asymmetry moment coefficient
C_{m_α}	Pitch moment coefficient derivative, 1/rad

C_{m_q}	Pitch damping moment coefficient based on qd/V, 1/rad
C_n	Yaw moment coefficient
C_{n_I}	Induced yaw moment coefficient
C_{n_β}	Yaw moment coefficient derivative, 1/rad
$C_{n_{p_\alpha}}$	Magnus moment coefficient derivative, 1/rad
C_N	Normal force coefficient
C_{N_F}	Fin normal force coefficient
$C_{N_{VORTEX}}$	Fin normal force coefficient due to body vortex
C_{N_I}	Induced normal force coefficient
C_{N_a}	Normal force coefficient derivative, 1/rad
C_Y	Yaw force coefficient
C_{Y_I}	Induced yaw force coefficient
C_{Y_β}	Yaw force coefficient derivative, 1/rad
d	Reference length and diameter, ft
I	Pitch moment of inertia, slug-ft^2
I_x	Roll moment of inertia, slug-ft^2
I_{sp}	Specific impulse, sec
K_w	Body-fin carryover factor
K_ϕ	Fin sweep-back factor
ℓ_γ	Total lift force derivative
M	Mach number
M_J	Joint compliance moment, lb-ft

m	Mass, slugs
m_i	Generalized mass
N	Number of fins
p	Roll rate, deg/sec
q	Pitch rate, deg/sec
$\bar{q}$	Dynamic pressure, lb/ft^2
R	57.3 deg/rad
r	Yaw rate, deg/sec
r_e	Distance from c.g. to nozzle throat, ft
r_o	$\left(r_e^2 - I/m\right)^{1/2}$
T	Thrust, lb
t	Time, sec
V	Velocity, ft/sec
X	Body station
X, Y, Z	Body axes
α	Angle of attack in body XZ plane, deg
α_T	Total angle of attack, deg
α_{TRIM}	Resonant trim angle of attack, deg
α_{ST}	Static trim angle of attack, deg
α^*	Angle of attack for which C_{ℓ_I} changes sign, deg
β	Angle of attack in body XY plane, deg
Γ	Angle defining the orientation of the c.g. offset, deg
Δcg	Center of gravity offset, in.
δ	Fin cant angle, deg
ϵ	Angular thrust misalignment, deg
$\hat{\epsilon}_i$	Generalized modal deflection
$\hat{\epsilon}_i'$	Generalized modal deflection slope
ξ, η, ζ	Elastic reference axes

μ	Angle defining the orientation of the thrust misalignment, deg
λ	Angle defining the orientation of the aerodynamic asymmetry, deg
λ_i	Generalized displacement of the ith mode
ω	Aerodynamic pitch frequency, $R\,(-C_{m_\alpha}\,\bar{q}Ad/I)^{1/2}$, deg/sec
ω_i	Generalized bending frequency
ϕ	Arc tan β/α, deg
ϕ	Fin elastic twist angle, deg
ψ	Phase angle, $\lambda-\phi$, deg
θ	Joint rotation angle, deg
τ	Rigid body coordinates
$[\ ]_E$	Elastic mode coefficient matrix
$[\ ]_T$	Rigid body mode coefficient matrix

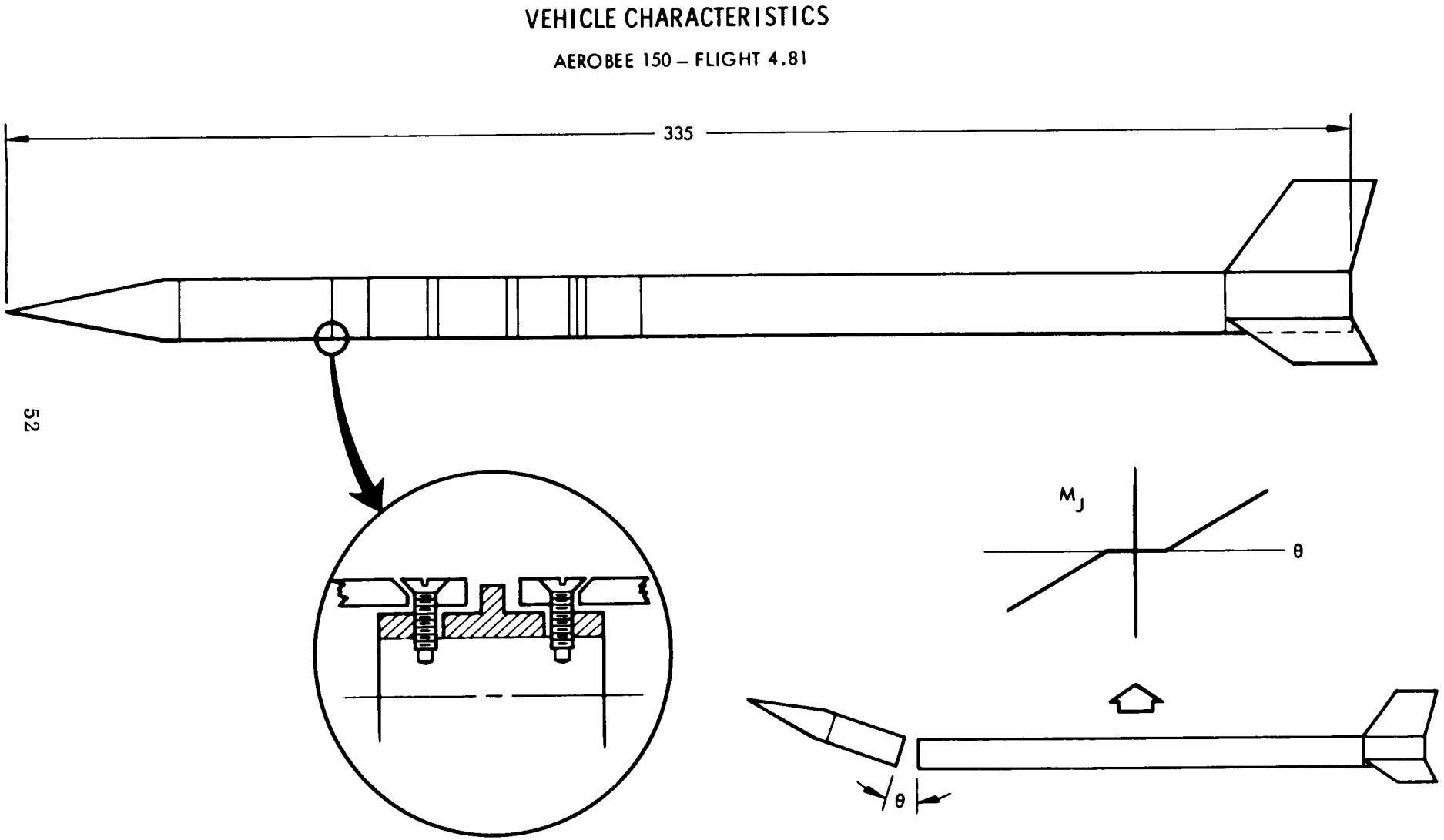

Fig. 1 Aerobee 150 Vehicle and Joint Characteristics - Flight No. 4.81

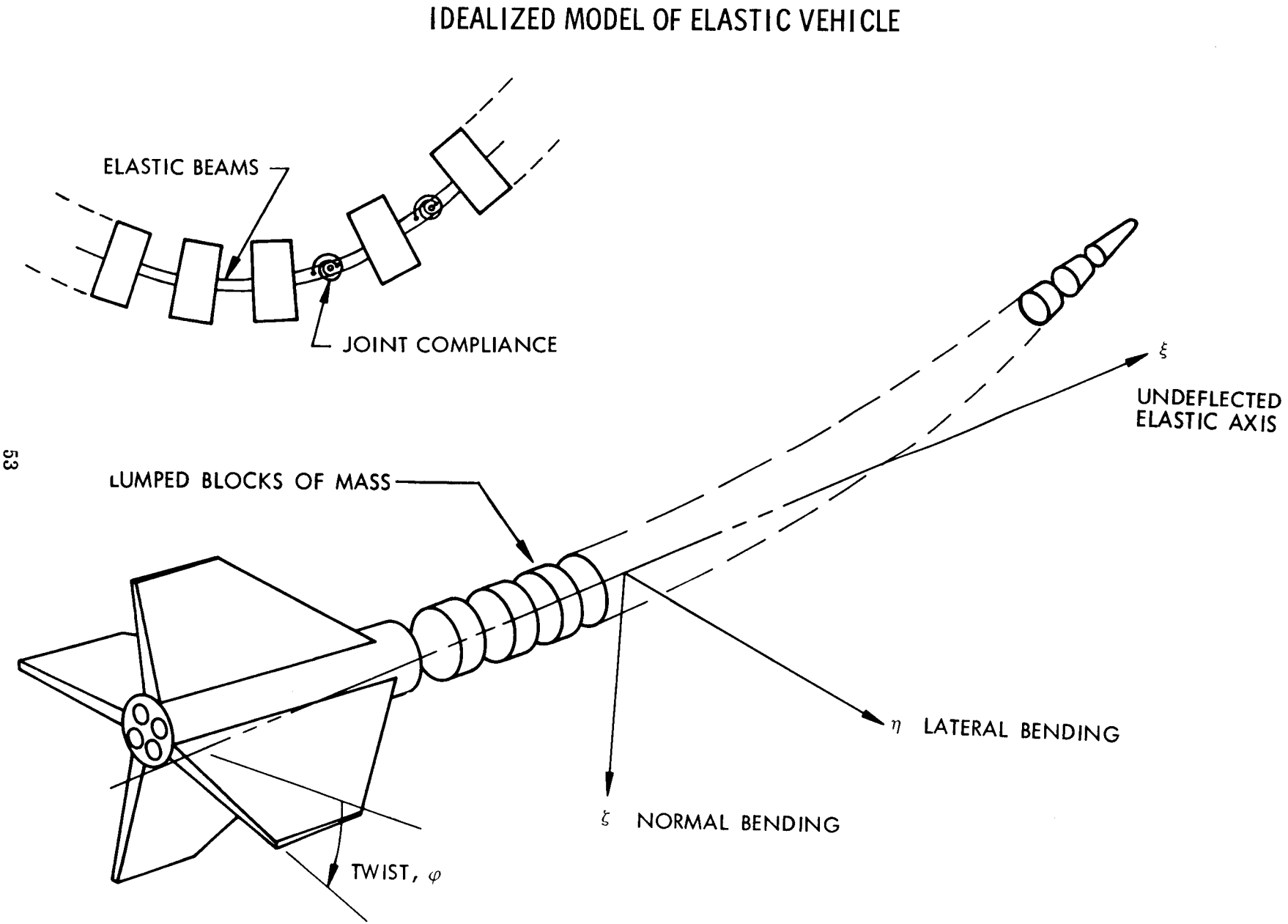

Fig. 2 I dealized Model of Elastic Vehicle and Joints

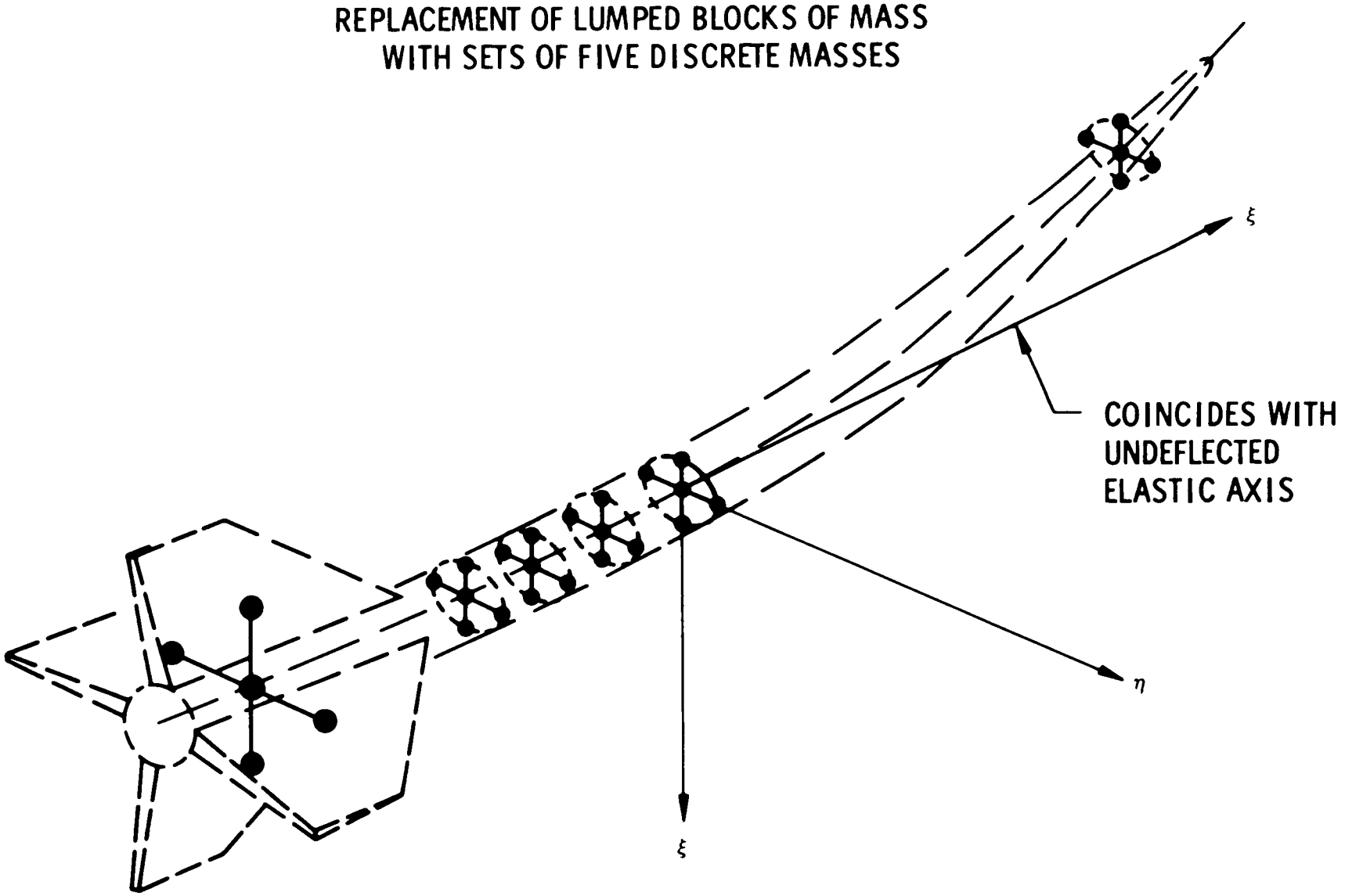

Fig. 3 Replacement of Lumped Blocks of Mass with Sets of Five Discrete Masses

EQUATIONS OF MOTION FOR ALL PARTICLES

$$\left[\left|\left[\begin{array}{c} m \end{array}\right]\right|, \left|\left[\begin{array}{c} \sigma_o \end{array}\right]\right|\right] \left|\begin{array}{c} \dot{\bar{v}} \\ \dot{\omega} \end{array}\right| - \left[\left|\left[\begin{array}{c} \omega \end{array}\right]\right|\left[\left|\left[\begin{array}{c} m \end{array}\right]\right|, \left|\left[\begin{array}{c} \sigma_o \end{array}\right]\right|\right]\right] \left|\begin{array}{c} \bar{v} \\ \omega \end{array}\right| - 2\left[\left|\left[\begin{array}{c} \omega \end{array}\right]\right|\right] \left|\left[\begin{array}{c} h_o \end{array}\right]\right|$$

$$- \left[\left|\left[\begin{array}{c} \ell_\gamma \end{array}\right]\right|\right] \left|\frac{1}{\bar{u}} \left|\left[\begin{array}{c} 1 \end{array}\right]\right| \left|\bar{v}\right| + \frac{1}{\bar{u}} \left|\left[\begin{array}{c} d_o \end{array}\right]\right| \left|\omega\right|\right| + \left[\left|\left[\begin{array}{c} m \end{array}\right]\right|\right] \left|\ddot{\epsilon}\right| + \left[\left|\left[\begin{array}{c} \mu \end{array}\right]\right|\right] \left|\dot{\epsilon}\right| + \left[\left|\left[\begin{array}{c} K \end{array}\right]\right|\right] \left|\epsilon\right|$$

$$- \left[\left|\left[\begin{array}{c} \ell_\gamma \end{array}\right]\right|\right] \left|\frac{1}{\bar{u}} \left|\dot{\underline{\epsilon}}\right| - \left|\underline{\epsilon}'\right|\right| - \left|\left[\begin{array}{c} P_o \end{array}\right]\right| \left|\rho\right|_E$$

$$- \left[\left|\left[\begin{array}{c} m \end{array}\right]\right|\right] \left[\left|\left[\begin{array}{c} \dot{\omega} \end{array}\right]\right|\right] \left|\epsilon\right| + \left[\left|\left[\begin{array}{c} \omega \end{array}\right]\right|\right] \left[\left|\left[\begin{array}{c} m \end{array}\right]\right|\right] \left[\left|\left[\begin{array}{c} \omega \end{array}\right]\right|\right] \left|\epsilon\right| - 2\left[\left|\left[\begin{array}{c} m \end{array}\right]\right|\right] \left[\left|\left[\begin{array}{c} \omega \end{array}\right]\right|\right] \left|\dot{\epsilon}\right|$$

$$-2\left[\left|\left[\begin{array}{c} \omega \end{array}\right]\right|\right]\left|\left[\begin{array}{c} h_o \end{array}\right]\right| \left|\rho\right|_E + \left[\left|\left[\begin{array}{c} \ell_\gamma \end{array}\right]\right|\right] \frac{1}{\bar{u}} \left[\left|\left[\begin{array}{c} \omega \end{array}\right]\right|\right] \left|\epsilon\right| = \left|\left|\begin{array}{c} p_o \end{array}\right|\right| + \left|\left|\begin{array}{c} \ell_o \end{array}\right|\right| + \left|\left[\begin{array}{c} m \end{array}\right]\right| \left|g\right|$$

ILLUSTRATING SEPARATION OF TERMS INTO COMPONENTS OF RIGID BODY TRANSLATION AND ROTATION, $\bar{v}$ AND ω ; GENERALIZED STRAIN $\left|\left|\begin{array}{c} \epsilon \end{array}\right|\right|$; AND CONSTANT TERMS $\left|\left|\begin{array}{c} p_o \end{array}\right|\right|$, $\left|\left|\begin{array}{c} \ell_o \end{array}\right|\right|$ AND $\left[\left|\left[\begin{array}{c} m \end{array}\right]\right|\right] \left|g\right|$.

Fig. 4 Equations of Motion for All Particles

FOR A "STEADY STATE" SOLUTION; VIZ. FOR CONDITION OF ROLL RESONANCE

$$\left| \begin{matrix} |\bar{v}| \\ |\omega| \end{matrix} \right| = \text{CONSTANT} \; ; \quad \left| |\epsilon| \right| = \text{CONSTANT} \; ; \quad |g| = \text{CONSTANT}$$

ASSUME:

1) ALL MASS, STRUCTURAL, AERODYNAMIC AND PROPULSION COEFFICIENTS = CONSTANTS
2) ENGINE THRUST = CONSTANT WITH HIGH I_{SP}
3) RESULTANT ROTATION VECTOR IS ALIGNED APPROXIMATELY WITH GRAVITY FIELD
4) $\bar{u} \approx V$; WITH V KNOWN, DROP DRAG EQUATION

USING PRINCIPAL OF VIRTUAL WORK; PRE-MULTIPLY EQUATION OF MOTION BY $\left[\{\hat{S}\} \right]$.

$$\left[\{\hat{S}\} \right] \left| |F| \right| = 0 = \begin{bmatrix} \{ [1] \} \\ \{ [d_o] \} \\ \{ \{\hat{\epsilon}\} \} \end{bmatrix} \left| |F| \right|$$

Fig. 5 Assumptions for Roll Resonance Condition

THE STEADY STATE SOLUTION

$$\left|\lambda\right| = [E]^{-1}\left|[A]\left|\begin{matrix}\bar{\gamma}\\ \omega\end{matrix}\right| + |C|\right|$$

WHERE:

$$[A] = \left[\{\{\hat{\epsilon}\}\}\right]\left[V\left[[\bar{\omega}]\right]\left|[m]\right| + \left[[\ell_\gamma]\right]\left|[1]\right|,\ \left[[\omega]\right]\left|[\sigma_o]\right| + \frac{1}{V}\left[[\ell_\gamma]\right]\left|[\underline{d}_o]\right| - 2\left|[h_o]\right| - V\left|[m]\right|\right]$$

$$|C| = \left[\{\{\hat{\epsilon}\}\}\right]\left|\left|p_o\right| + \left|\ell_o\right| + \left|[m]\right|\,|g|\right|$$

$$[E] = \left[\{\{\hat{\epsilon}\}\}\right]\left[\left[[K]\right] + \left[[\omega]^2\right]\left[[m]\right] + \frac{1}{V}\left[[\ell_\gamma]\right]\left[[\underline{\omega}]\right]\right]\left[\left|\hat{\epsilon}\right|\right]$$

$$- \left[\left|[p_o]\right| + 2\left[[\omega]\right]\left|[h_o]\right|\right]\left[\hat{\rho}\,E\right] + \left[[\ell_\gamma]\right]\left[\left|\epsilon'\right|\right]$$

THE MODIFIED RIGID BODY EQUATIONS BECOME

$$-[B]\left|\begin{matrix}\bar{\gamma}\\ \omega\end{matrix}\right| + [F][E]^{-1}\left|[A]\left|\begin{matrix}\bar{\gamma}\\ \omega\end{matrix}\right| + C\right| = D$$

WHICH MAY BE ARRANGED IN THE FINAL FORM

$$\left[\underbrace{[F][E]^{-1}[A]}_{\text{ELASTIC INCREMENT TO LIFT \& MOMENT}} - \underbrace{[B]\left|\begin{matrix}\bar{\gamma}\\ \omega\end{matrix}\right|}_{\text{RIGID BODY}}\right] \quad D - \underbrace{[F][E]^{-1}C}_{\text{ELASTIC INCREMENT TO LIFT \& MOMENT}}$$

Fig. 6a The Steady State Solution for Elastic Increments to Lift and Moment

THE "FIRST TWO" MATRIX EQUATIONS FROM THE PRINCIPAL OF VIRTUAL WORK

$$-\left[B\right]\left|\begin{matrix}|\bar{\gamma}|\\ |\omega|\end{matrix}\right| + \left[F\right]|\lambda| = |D|$$

WHERE

$$\left[B\right] = \begin{bmatrix}\{[1]\}\\ \{[d_o]'\}\end{bmatrix}\left[V\left[\left[\omega\right]\right]\left|\left[m\right]\right| + \left[\left[\ell_\gamma\right]\right]\left|\left[1\right]\right| \;,\; \left[\left[\omega\right]\right]\left|\left[\sigma_o\right]\right| + \frac{1}{V}\left[\left[\ell_\gamma\right]\right]\left|\left[\underline{d}_o\right]\right| - 2\left|\left[h_o\right]\right| - V\left|\left[\;m\;\right]\right|\right]$$

$$|D| = \begin{bmatrix}\{[1]\}\\ \{[d_o]'\}\end{bmatrix}\left|\left|\,|p_o|\right| + \left|\,|\ell_o|\right| + \left|\left[m\right]\right||g|\right|$$

$$\left[F\right] = \begin{bmatrix}\{[1]\}\\ \{[d_o]'\}\end{bmatrix}\left[\left[\left[\left[K\right]\right] + \left[\left[\omega\right]^2\right]\left[\left[m\right]\right] + \frac{1}{V}\left[\left[\ell_\gamma\right]\right]\left[\left[\underline{\omega}\right]\right]\right]\left[\left|\,|\hat{\epsilon}|\right|\right]\right.$$

$$\left. - \left[\left|\left[p_o\right]\right| + 2\left[\left[\omega\right]\right]\left|\left[h_o\right]\right|\right]\left[|\hat{\rho}|_E\right] + \left[\left[\ell_\gamma\right]\right]\left[\left|\,|\hat{\epsilon}|'\right|\right]\right]$$

Fig. 6b The Steady State Solution for Elastic Increments to Lift and Moment

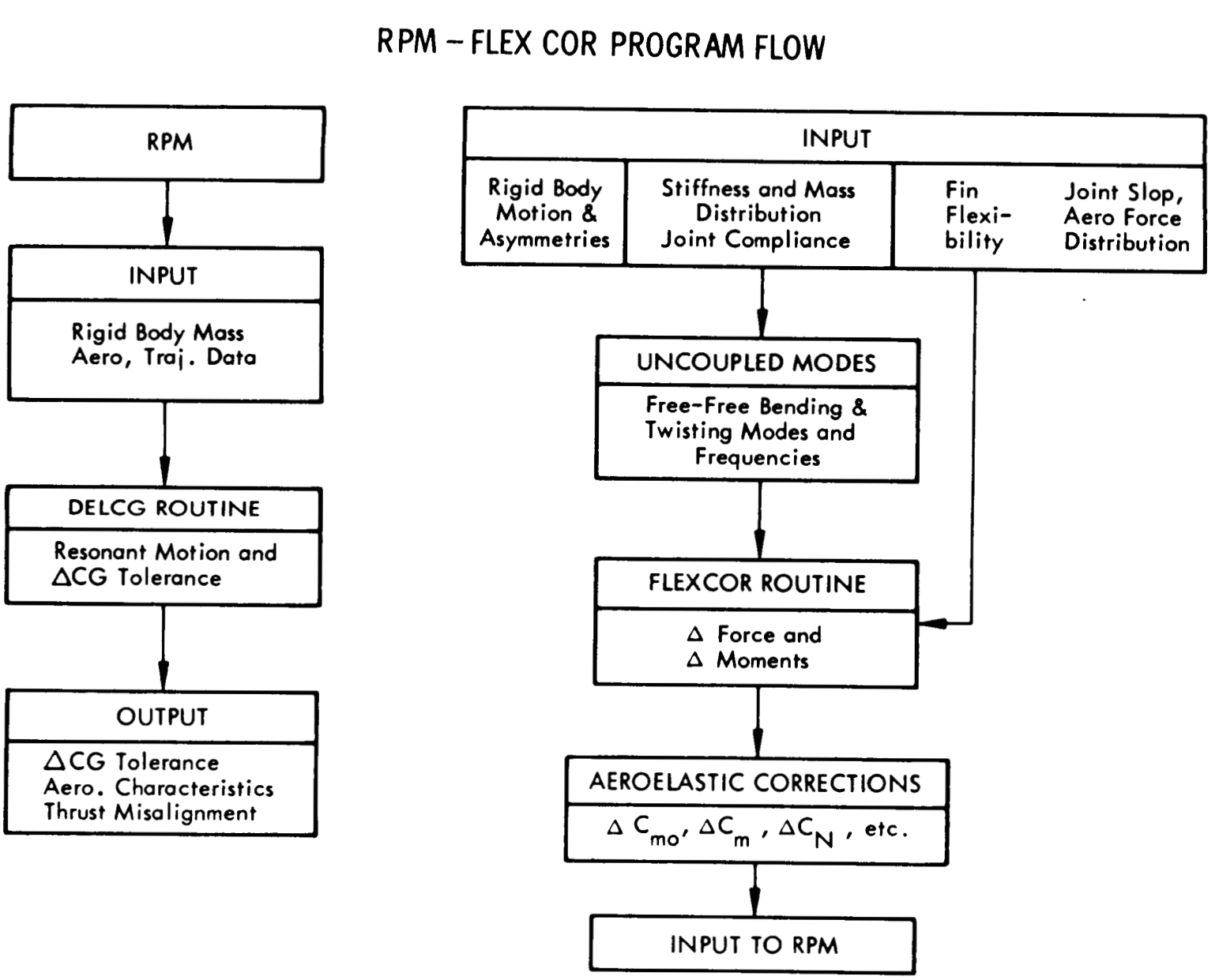

Fig. 7 Computer Program Flow Diagram for Rigid Body RPM and Elastic Correction FLEXCOR

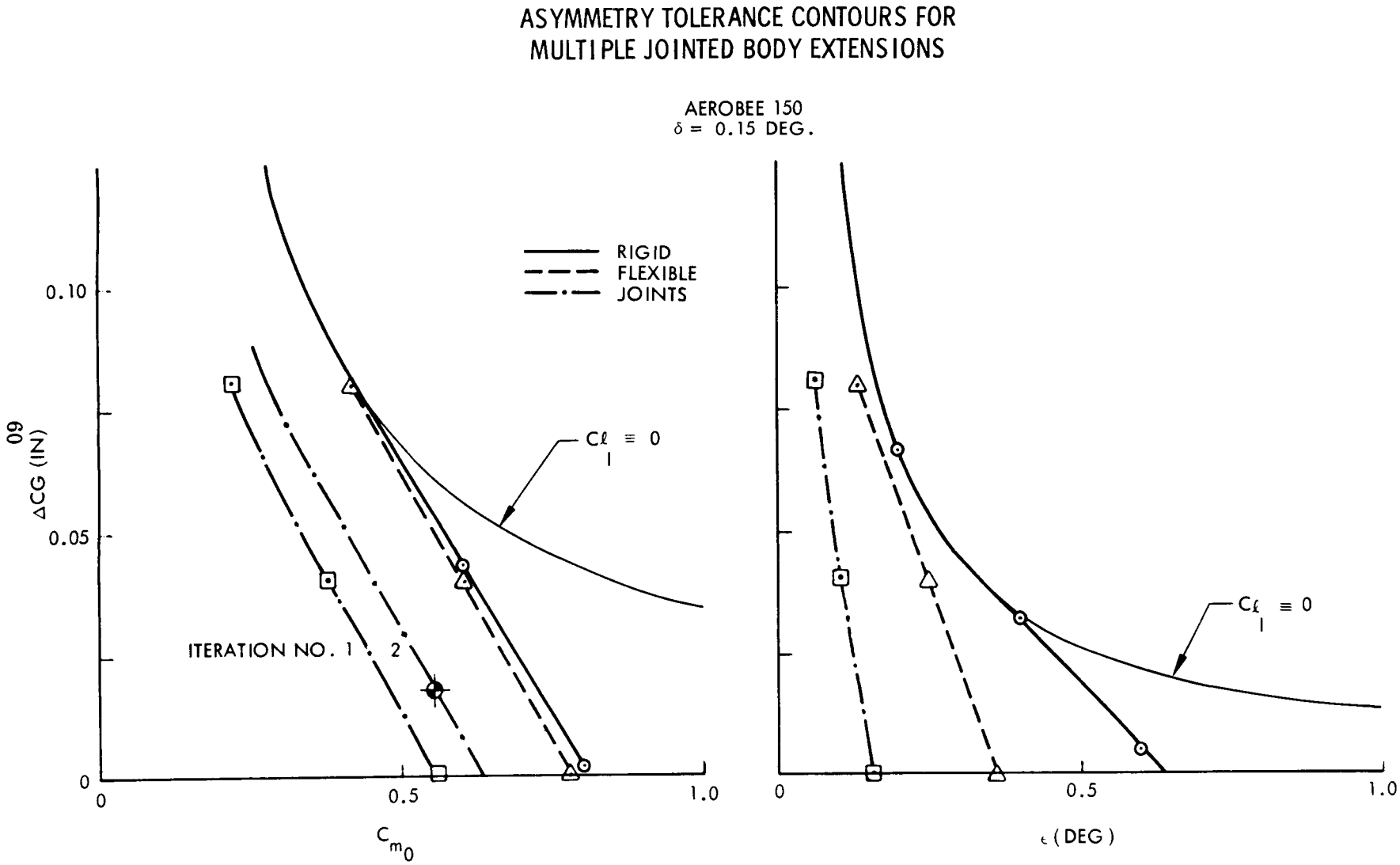

Fig. 8 Asymmetry Tolerance Contours for Multiple Jointed Body Extensions – Aerobee 150

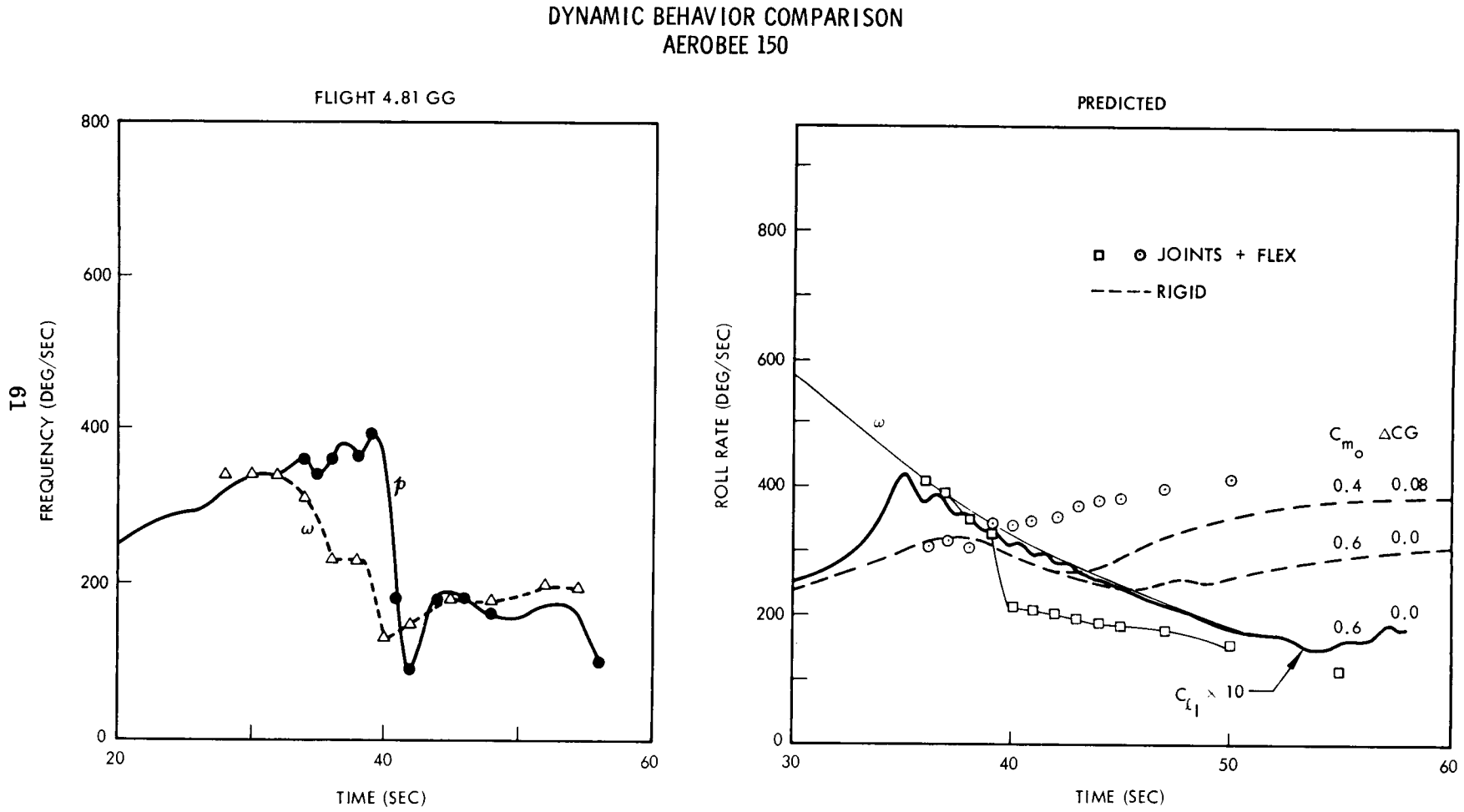

Fig. 9 Flight Behavior Comparison Aerobee 100 With 12 Joints

METHOD FOR ASSESSING FIN FLEXIBILITY EFFECTS

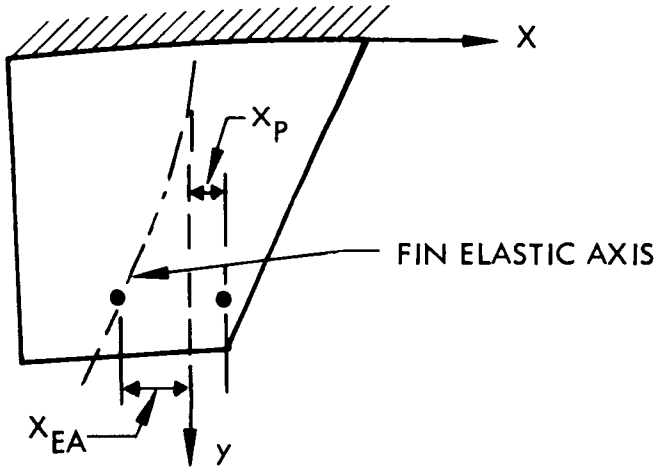

BENDING-TORSION METHOD

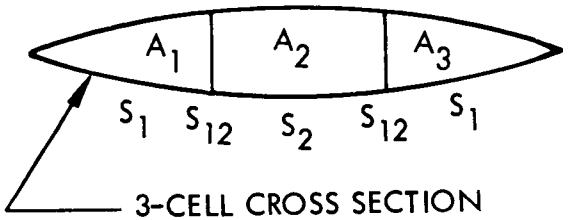

TORQUE-BOX METHOD

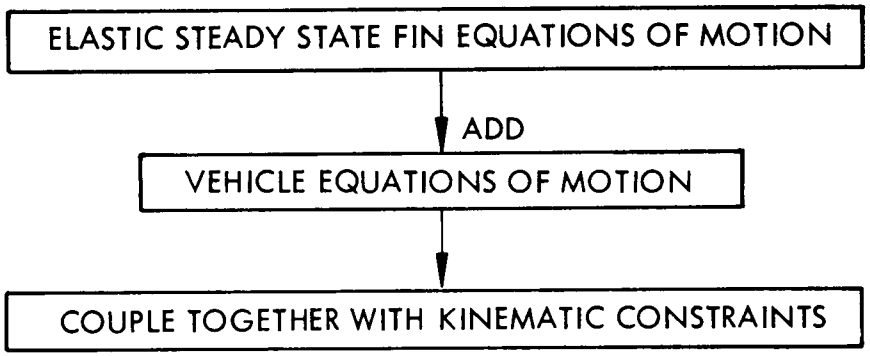

Fig. 10 Fin Flexure Models

METHOD FOR ASSESSING FIN FLEXIBILITY EFFECTS

APPLY PRINCIPLE OF VIRTUAL WORK TO COUPLED EQUATIONS IN ORDER TO ELIMINATE ELASTIC DEGREES OF FREEDOM

$$\left[[A]_{\tau}^{E} \left[[A]_{E}^{E} \right]^{-1} [A]_{E}^{\tau} - [A]_{\tau}^{\tau} \right] |\tau| = |B|_{\tau} - [A]_{\tau}^{E} \left[[A]_{E}^{E} \right]^{-1} |B|_{E}$$

RIGID VEHICLE

ELASTIC CORRECTIONS

WHERE: $|\tau|$ = COORDINATES OF RIGID BODY MOTION OF VEHICLE C.G.

$[A]_{\tau}^{E}$, $[A]_{E}^{E}$, $|B|_{E}$, ETC. = COEFFICIENTS OF ELASTIC MODES

$[A]_{\tau}^{\tau}$, $|B|_{\tau}^{\tau}$ = COEFFICIENTS OF RIGID VEHICLE MODES, PITCH, YAW. ROLL, PLUNGE, SLIDESLIP

Fig. 11 Method for Assessing Fin Flexibility Effects

FLOW INTERACTION CHARACTERISTICS

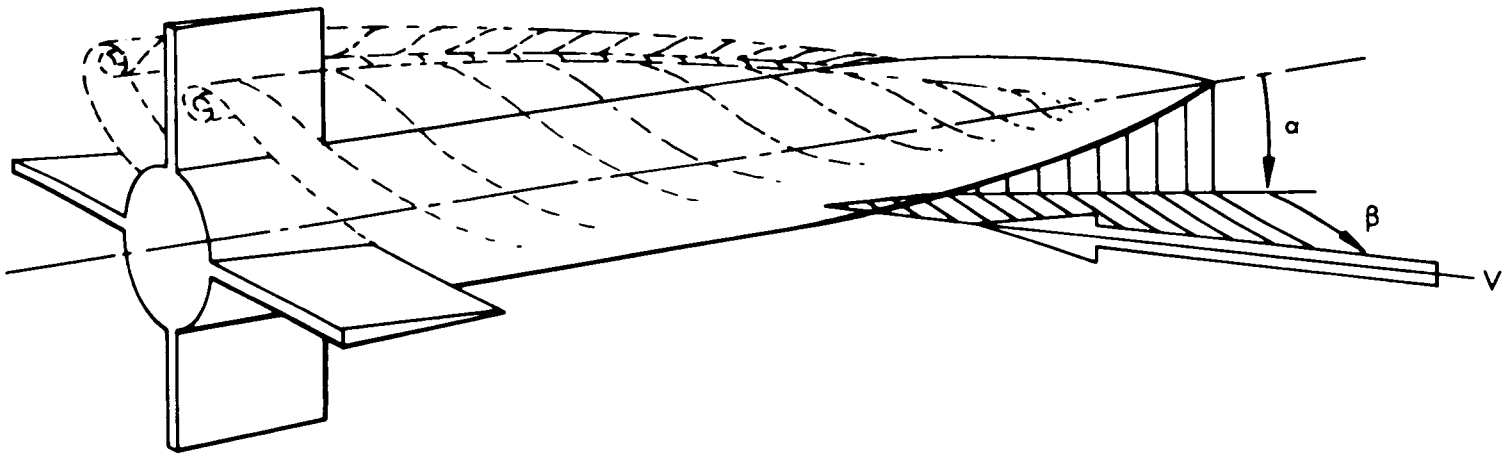

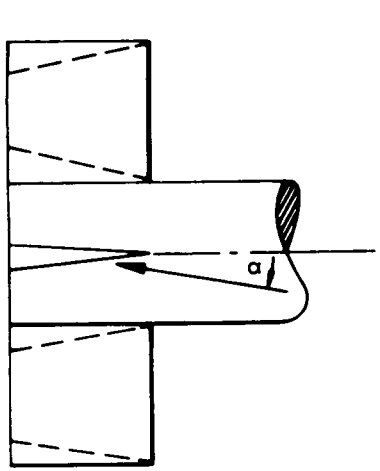

FIN + BODY

$C_{N_F} = C_{N_{\alpha_F}} K_W \alpha$

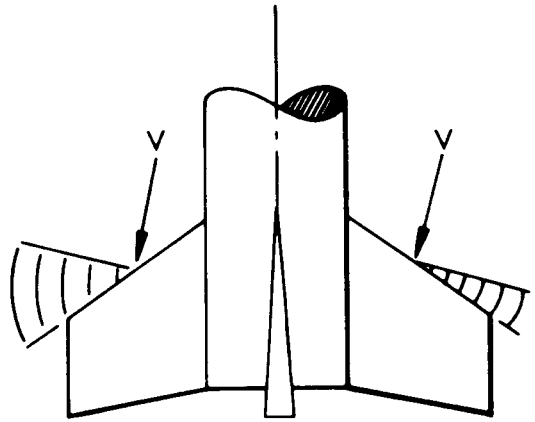

SWEEPBACK

$+ C_{N_\alpha} (K_\phi \cot \& \beta) \alpha$

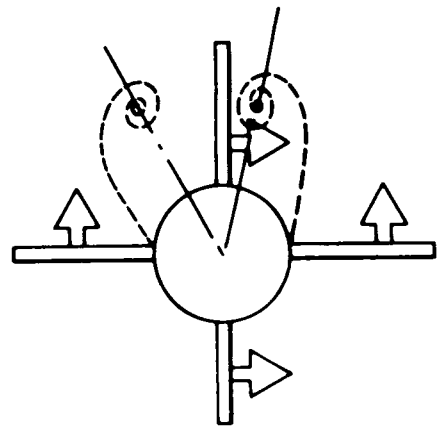

VORTEX

$+ C_{N_{VORTEX}}$

Fig. 12 Flow Interaction Characteristics

FIN AERODYNAMIC CHARACTERISTICS

M = 2
α = 20 DEG.

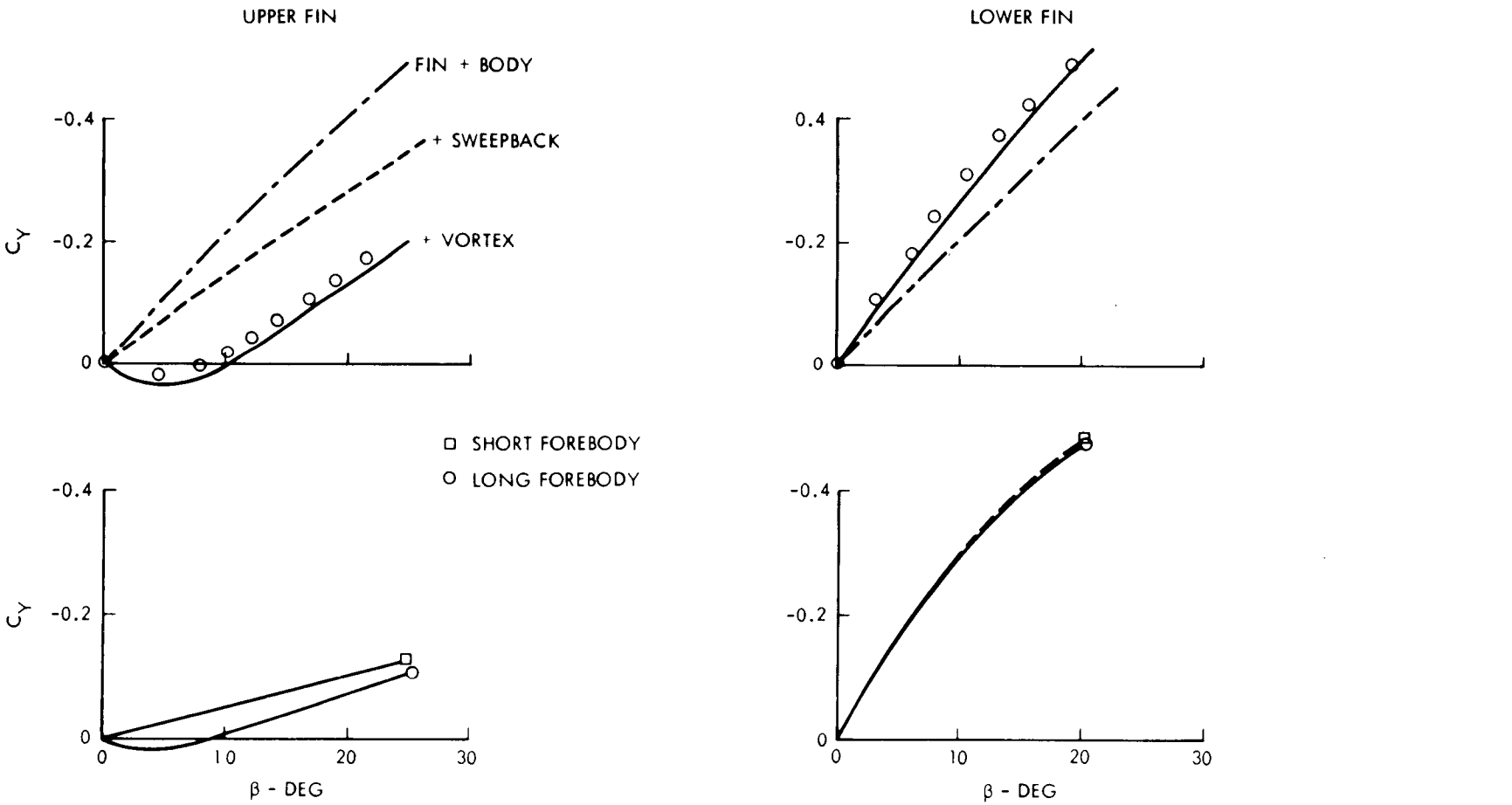

REF: NASA RM A57E21

Fig. 13 Fin Aerodynamic Characteristics

VEHICLE AERODYNAMIC CHARACTERISTICS

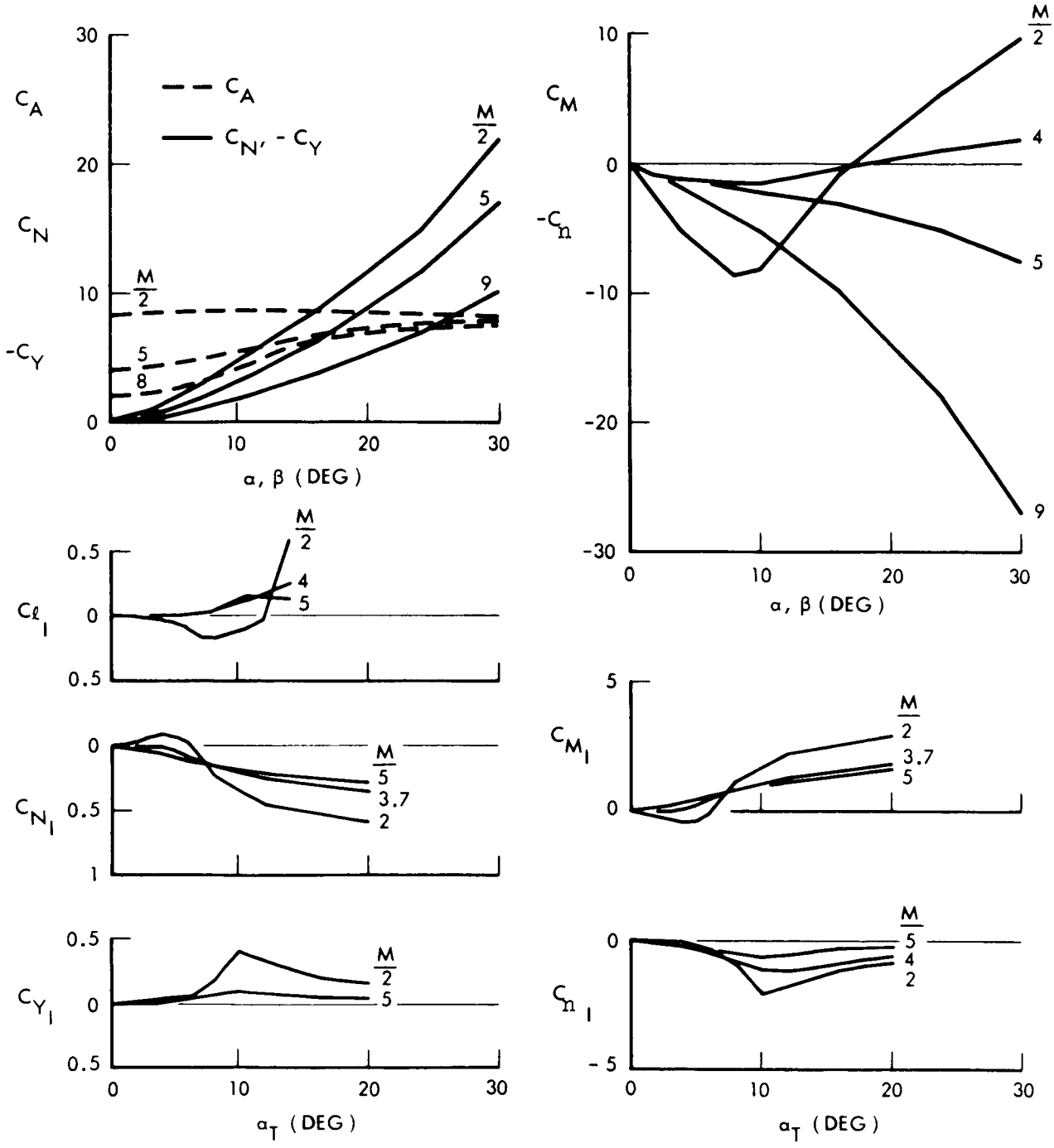

Fig. 14 Aerobee 350 Vehicle Non-Linear and Induced Aerodynamic Characteristics

EQUATIONS OF MOTION WITH NON-LINEAR AND INDUCED AERODYNAMIC CHARACTERISTICS

$$\ddot{\beta} + A_{11}\dot{\beta} - A_{21}\dot{\alpha} - B_{11}\beta + B_{21}\alpha = C_1$$

$$\ddot{\alpha} + A_{12}\dot{\alpha} + A_{22}\dot{\beta} - B_{12}\alpha - B_{22}\beta = C_2$$

$$p = \frac{\bar{q}\,Ad}{I_x}\left|C_{l_\delta}\,\delta + C_{l_p}\frac{pd}{2V} + C_{l_I}\sin N\phi - \frac{\Delta CG}{12d}\left|C_N\cos\Gamma + C_Y\sin\Gamma\right|\right|$$

$$A_{11} = \frac{\bar{q}A}{mV}\left|C_{Y_\beta} - \frac{md^2}{I}C_{n_r}\right| + \frac{T}{mV} + \frac{r_o^2\,T}{gI\,Isp} \quad ; \quad A_{21} = p\left|2 - \frac{I_x}{I}\right|$$

$$A_{12} = \frac{\bar{q}A}{mV}\left|C_{L_\alpha} - \frac{md^2}{I}C_{m_q}\right| + \frac{T}{mV} + \frac{T\,r_o^2}{gI\,Isp} \quad ; \quad A_{22} = p\left|2 - \frac{I_x}{I}\right|$$

$$B_{11} = -\frac{C_n}{\beta}\frac{\bar{q}\,Ad}{I} + p^2\left|1 - I_x/I\right| \quad ; \quad C_1 = \left|C_{m_o}\cos\lambda - C_A\frac{\Delta CG}{d}\sin\Gamma\right|\frac{\bar{q}\,Ad}{I} + \frac{T\epsilon r_e}{I}\cos\mu$$

$$B_{12} = \frac{C_m}{\alpha}\frac{\bar{q}\,Ad}{I} + p^2\left|1 - I_x/I\right| \quad ; \quad C_2 = \left|C_{m_o}\sin\lambda - C_A\frac{\Delta CG}{d}\cos\Gamma\right|\frac{\bar{q}\,Ad}{I} + \frac{T\epsilon r_e}{I}\sin\mu$$

Fig. 15 Equations of Motion With Non-Linear and Induced Aerodynamic Characteristics

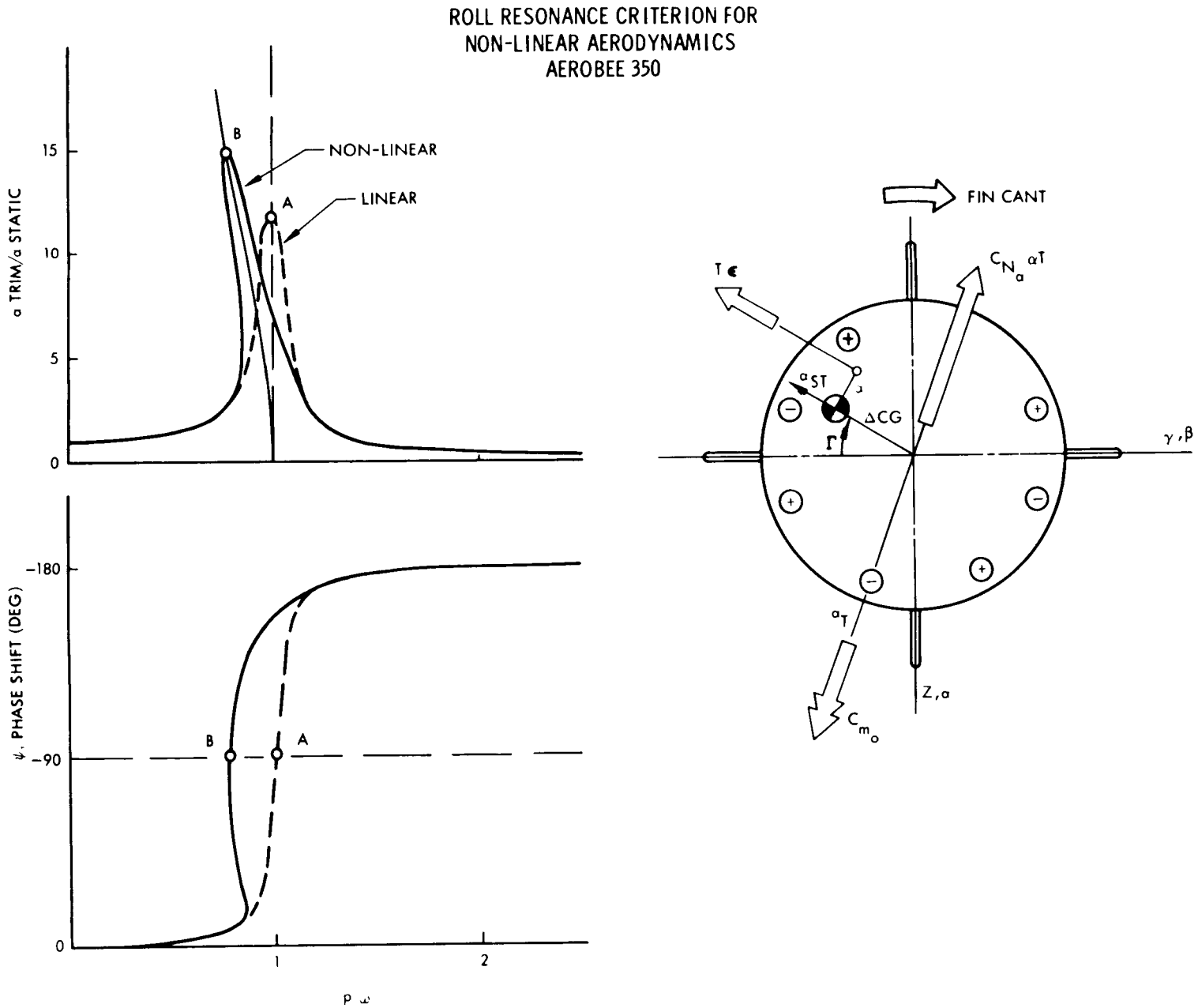

Fig. 16 Roll Resonance Criterion for Non-Linear Aerodynamics – Aerobee 350

RESONANT TRIM SOLUTION WITH NON-LINEAR AND INDUCED AERODYNAMIC CHARACTERISTICS

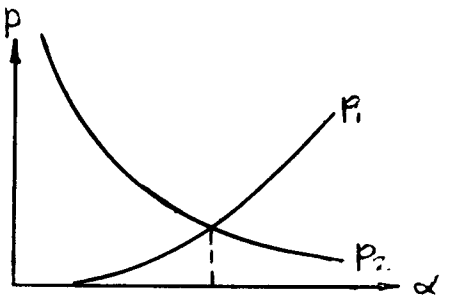

(1) $-B_{11}\beta + B_{21}\alpha = C_1$ $\qquad \beta = \alpha_T \sin\varphi$

(2) $-B_{12}\alpha - B_{22}\beta = C_2$ $\qquad \alpha = \alpha_T \cos\varphi$

(1) $\sin\varphi$ + (2) $\cos\varphi$ YIELDS:

$$\left\{C_n \sin\varphi - C_m \cos\varphi\right\}\frac{\bar{q}\,Ad}{I} + p^2\,(1 - I_x/I)\,\alpha_T - p\,\frac{\bar{q}A}{mV}\left\{\left[C_{L_I}\sin\phi - C_{y_I}\cos\phi\right](1 - I_x/I)\right\} = 0$$

$$p_1^2 = \left\{C_n \sin\Gamma - C_m \cos\Gamma\right\}\frac{\bar{q}\,Ad}{(I - I_x)\,\alpha_T}$$

(1) $\cos\varphi$ - (2) $\sin\varphi$ YIELDS:

$$\frac{\bar{q}\,Ad}{I}\left\{C_{n_I}\sin N\phi\cos\varphi + C_{m_Z}\sin\frac{N}{2}\varphi\sin\varphi\right\} - p\,\frac{\bar{q}A}{mV}\left\{\left|C_L\cos\varphi + C_y\sin\phi\right|\right.$$

$$\left.\times\left(1 - \frac{I_x}{I}\right) - \frac{md^2}{I}C_{m_q}\alpha_T\right\} - \alpha_{T_p}\left\{\frac{T(1 - I_x/I)}{mV} + \frac{Tr_o^2}{gIIsp}\right\} = \left\{C_{m_o} - C_A\frac{\Delta CG}{d}\right\}\frac{\bar{q}\,Ad}{I} + \frac{T\epsilon r_o}{I}$$

$$p_2 = \frac{\left\{C_{m_o} - C_A\frac{\Delta CG}{d}\right\}\frac{\bar{q}\,Ad}{I} + \frac{T\epsilon r_o}{I}}{\frac{\bar{q}A}{mV}\left\{\left|C_L\cos\Gamma + C_y\sin\Gamma\right|\left(1 - \frac{I_x}{I}\right) - \frac{md^2}{I}C_{m_q}\alpha_T\right\} + \left\{\frac{T\left(1 - \frac{I_x}{I}\right)}{mV} + \frac{Tr_o^2}{gIIsp}\right\}\alpha_T}$$

Fig. 17 Resonant Trim Solution with Non-Linear and Induced Aerodynamic Characteristics

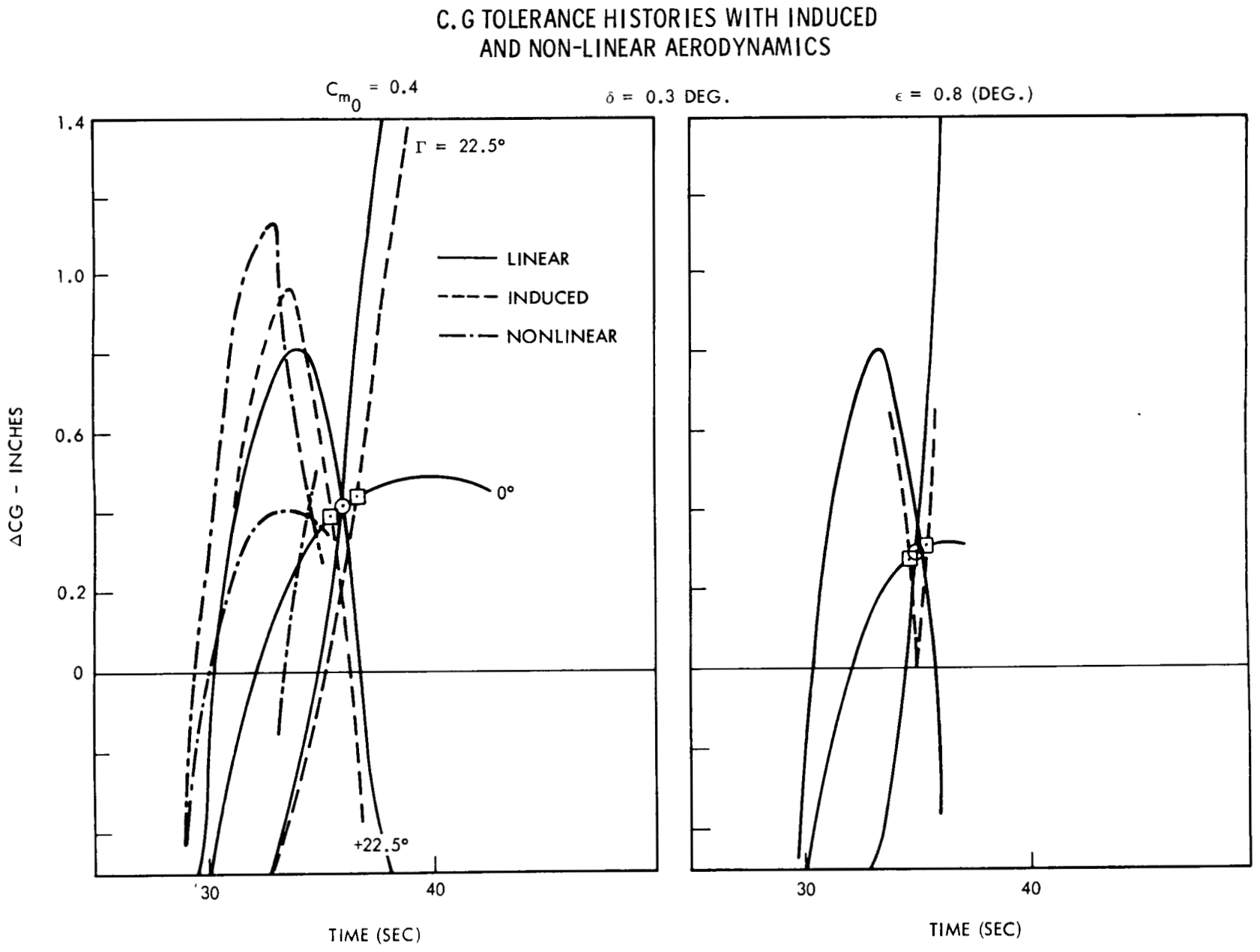

Fig. 18 C. G. Tolerance Histories with Induced and Non-Linear Aerodynamics – Aerobee 350

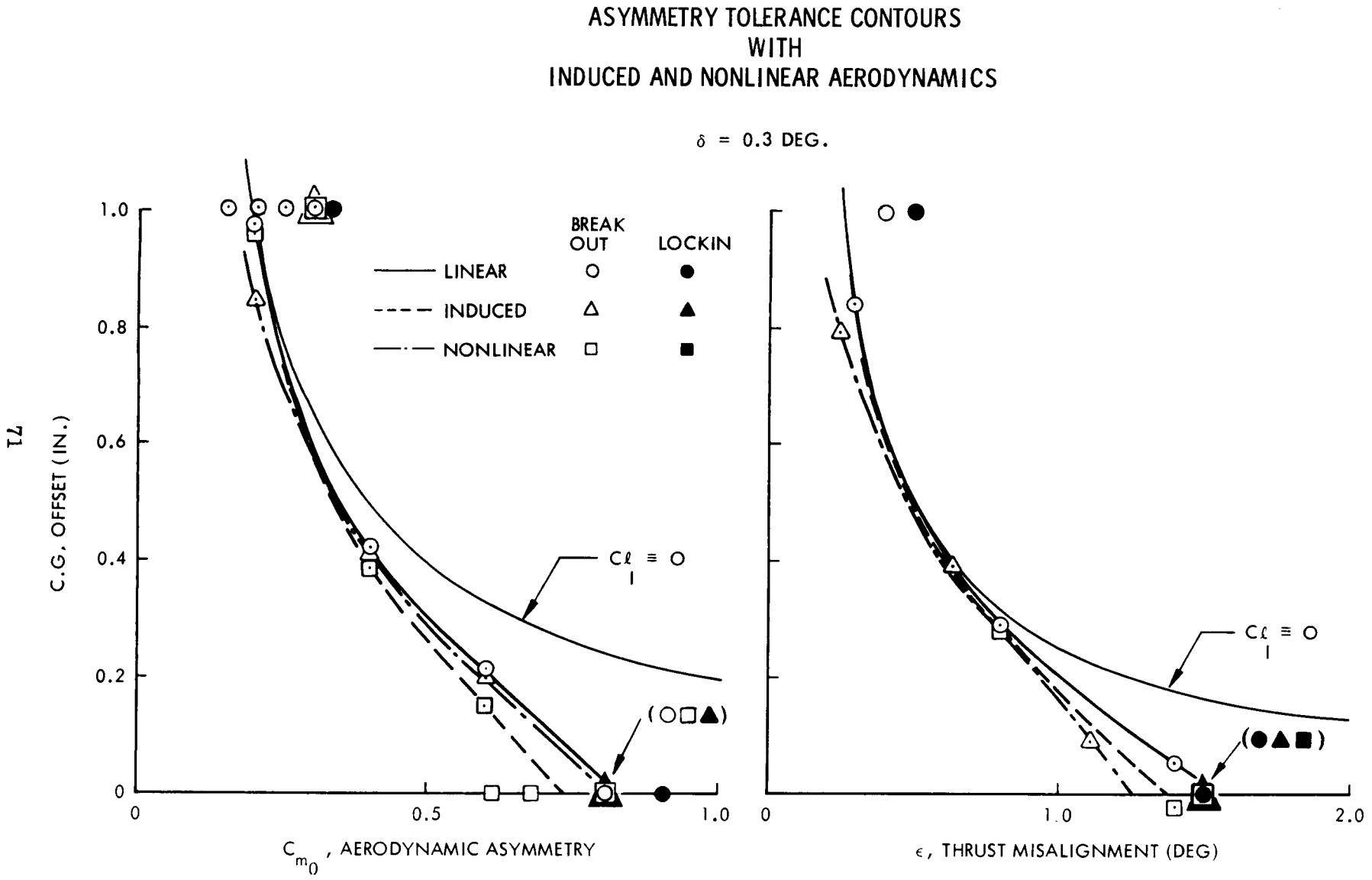

Fig. 19 Asymmetry Tolerance Contours with Induced and Non-Linear Aerodynamic Characteristics

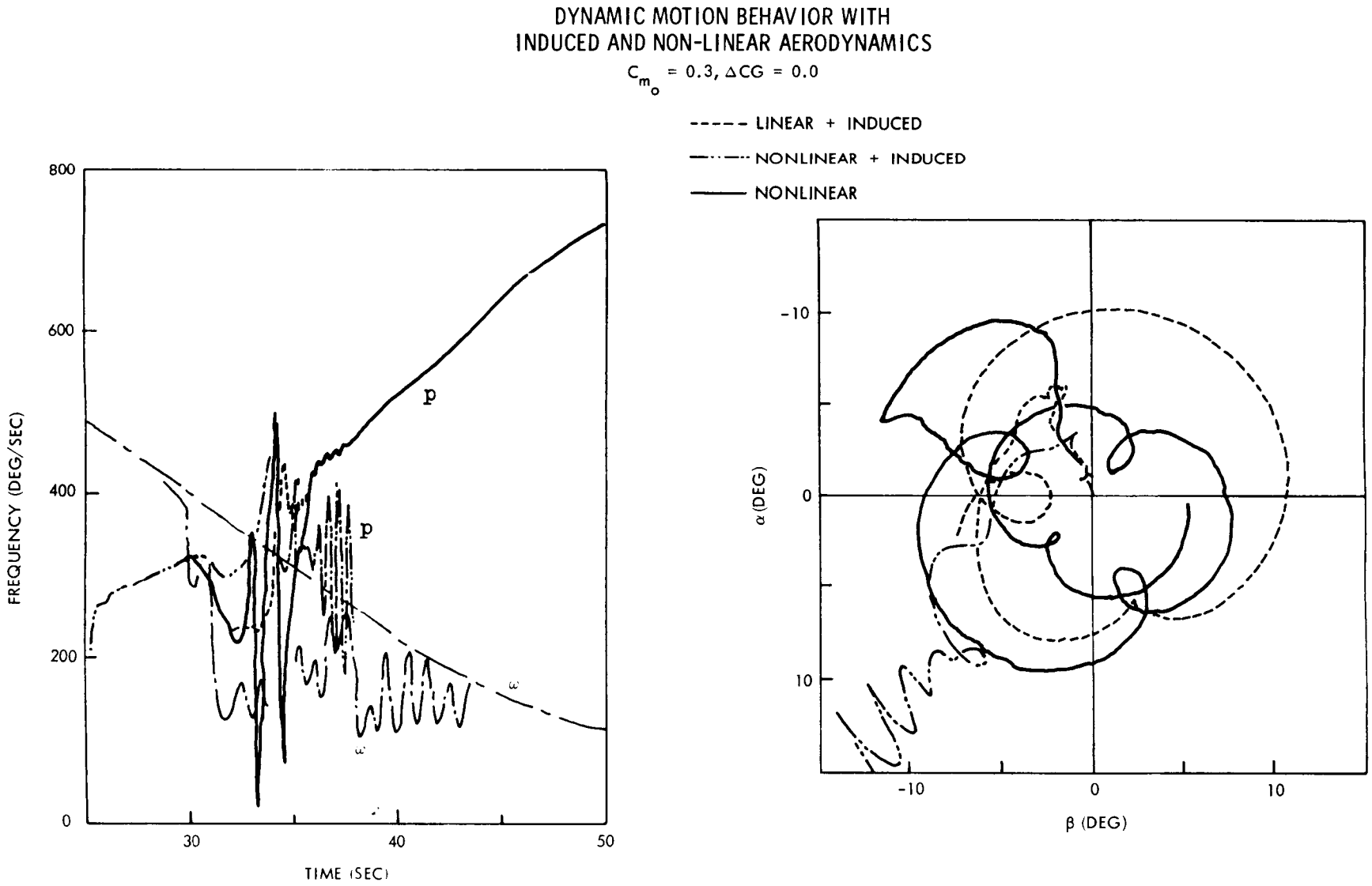

Fig. 20 Dynamic Motion Behavior with Induced and Non-Linear Aerodynamic Characteristics

APPENDIX I – DESCRIPTION OF MODIFIED ROLL-PITCH MOTION (RPM) COMPUTER PROGRAM

The basic format of the RPM program described in Ref. 2, is unchanged. Two options are available:

1) Dynamic motion – integrates the body referenced angle of attack, side slip and roll angle equations of motion of Fig. 15 about a predetermined trajectory.

2) Center of gravity tolerance – calculates the c.g. offset history required to maintain steady state resonance throughout the trajectory for the asymmetry orientation yielding the maximum roll rate retardation (Equations of Fig. 17).

The program consists of nine subprograms as follows:

MAIN PROGRAM – Controls program flow, reads input data, initializes parameters, starts and stop integration procedure, monitors critical variable limits.

BIGSUB – Performs time integration of variables, for dynamic option, adjusts computation time interval to maintain accuracy within prescribed limits. Minimum and maximum time interval can be specified.

CALC – Calculates constant coefficients used throughout the trajectory.

TABLOK – Performs linear interpolation of 1) vehicle and trajectory input data with time and 2) aerodynamic data with Mach number and angle of attack or sideslip or resultant angle of attack for magnitude and local slope with angle.

WRITE – Formats and transfer output data for listing

SETUP – Calculates coefficients for equations of motion, variable accelerations and store plot data for the dynamic motion option

GRAPH – Formats and transfers output data for plotting dynamic motion variables (inertial attitude locus, $\alpha - \beta$ locus, α_1 vs. t and p vs. t) on Stromberg-Carlson 4020 plotter.

DELCG – Calculates steady state angle of attack and roll rate for roll resonance and c.g. offset requires to maintain roll resonance.

PLOT – Formats and transfers output data for plotting up to 5 separate c.g. offset histories (Δcg vs. t) on the Stromberg Carlson 4020 plotter.

CURTIM – Prints current time at beginning and end of each run.

INPUT FORMAT – The input data are arranged in blocks of six words in 6E12 format except for trajectory and aerodynamic tables. Each block is controlled by header card in 4I3 format giving the number of the block, first word through last word to be read, and variable index number where applicable. A blank control card terminates the data read and starts the calculation. Successive runs are made by overloading only those data to be changed followed by a blank. The machine computations are terminated by a block number of 999.

The FORTRAN listing and sample input/output may be obtained from the authors of this report.